

Carbon and oxygen abundances in stellar populations $\star, \star \star$

P. E. Nissen^{1,2}, Y. Q. Chen¹, L. Carigi³, W. J. Schuster⁴, and G. Zhao¹

¹ Key Laboratory of Optical Astronomy, National Astronomical Observatories, Chinese Academy of Sciences, Beijing, 100012, China.

² Stellar Astrophysics Centre, Department of Physics and Astronomy, Aarhus University, Ny Munkegade 120, DK-8000 Aarhus C, Denmark. e-mail: pen@phys.au.dk

³ Instituto de Astronomía, Universidad Nacional Autónoma de México, AP 70-264, 04510 México DF, Mexico

⁴ Observatorio Astronómico Nacional, Universidad Nacional Autónoma de México, Apartado Postal 877, C.P. 22800 Ensenada, B.C., Mexico.

Received 12 May 2014 / Accepted 17 June 2014

ABSTRACT

Context. Carbon and oxygen abundances in stars are important in many fields of astrophysics including nucleosynthesis, stellar structure, evolution of galaxies, and formation of planetary systems. Still, our knowledge of the abundances of these elements in different stellar populations is uncertain because of difficulties in observing and analyzing atomic and molecular lines of C and O.

Aims. Abundances of C, O, and Fe are determined for F and G main-sequence stars in the solar neighborhood with metallicities in the range $-1.6 < [\text{Fe}/\text{H}] < +0.4$ in order to study trends and possible systematic differences in the C/Fe, O/Fe, and C/O ratios for thin- and thick-disk stars as well as high- and low-alpha halo stars. In addition, we investigate if there is any connection between C and O abundances in stellar atmospheres and the occurrence of planets.

Methods. Carbon abundances are determined from the $\lambda\lambda 5052, 5380$ C I lines and oxygen abundances from the $\lambda 7774$ O I triplet and the forbidden [O I] line at 6300 \AA . MARCS model atmospheres are applied and non-LTE corrections for the O I triplet are included.

Results. Systematic differences between high- and low-alpha halo stars and between thin- and thick-disk stars are seen in the trends of [C/Fe] and [O/Fe]. The two halo populations and thick-disk stars show the same trend of [C/O] versus [O/H], whereas the thin-disk stars are shifted to higher [C/O] values. Furthermore, we find some evidence of higher C/O and C/Fe ratios in stars hosting planets than in stars for which no planets have been detected.

Conclusions. The results suggest that C and O in both high- and low-alpha halo stars and in thick-disk stars are made mainly in massive ($M > 8M_{\odot}$) stars, whereas thin-disk stars have an additional carbon contribution from low-mass AGB and massive stars of high metallicity causing a rising trend of the C/O ratio with increasing metallicity. However, at the highest metallicities investigated ($[\text{Fe}/\text{H}] \approx +0.4$), C/O does not exceed 0.8, which seems to exclude formation of carbon planets if proto-planetary disks have the same composition as their parent stars.

Key words. stars: abundances – stars: atmospheres – (stars:) planetary systems – Galaxy: disk – Galaxy: halo

1. Introduction

Next to hydrogen and helium, carbon and oxygen are the most abundant elements in the Universe, and their abundances are of high importance in many fields of astrophysics, for example stellar age determinations (Bond et al. 2013), chemical evolution of galaxies (Chiappini et al. 2003; Carigi et al. 2005; Cescutti et al. 2009), and structure of exoplanets (Bond et al. 2010; Madhusudhan 2012).

While it is generally accepted that oxygen is produced by hydrostatic burning in massive stars and then dispersed to the interstellar medium in SNeII explosions (e.g., Kobayashi et al. 2006), the origin of carbon is more uncertain. Both massive ($M > 8M_{\odot}$) and low- to intermediate-mass stars probably contribute, but their relative importance and yields are not well known due to

uncertainties about metallicity-dependent mass loss (Meynet & Maeder 2002; van den Hoek & Groenewegen 1997).

The nucleosynthesis and Galactic evolution of C and O may be studied by determining abundances in F, G, and K stars with different ages and metallicities. There is, however, still considerable uncertainty about the abundances of C and O, because the available atomic and molecular lines provide diverging results depending on non-LTE corrections and atmospheric models applied (Asplund 2005). In the case of oxygen, all studies show a rising trend of the oxygen-to-iron ratio as a function of decreasing iron abundance, but the derived level of [O/Fe]¹ among metal-poor halo star ranges from 0.4 dex to 0.8 dex, corresponding to more than a factor of two in the O/Fe ratio (Nissen et al. 2002; Fulbright & Johnson 2003; Cayrel et al. 2004; García Pérez 2006; Ramírez et al. 2013). Carbon, on the other hand, follows iron more closely than oxygen, but some studies suggest small deviations from the solar C/Fe ratio in low-metallicity disk and halo stars (Gustafsson et al. 1999; Shi et al. 2002; Reddy et al. 2006; Fabbian et al. 2009; Takeda & Takada-Hidai 2013).

* Based on observations made with the Nordic Optical Telescope and on data products from observations made with ESO Telescopes at the La Silla Paranal Observatory under programs given in Table 2 and in Tables 1 and 2 of Nissen & Schuster (2010).

** Tables 2, 3, 4, and 5 are provided as online material and are also available at the CDS via anonymous ftp to cdsarc.u-strasbg.fr (130.79.128.5a) or via <http://cdsarc.u-strasbg.fr/viz-bin/qcat?/A+A/XXX/xxx>.

¹ For two elements, X and Y, with number densities N_X and N_Y , $[\text{X}/\text{Y}] \equiv \log(N_X/N_Y)_{\text{star}} - \log(N_X/N_Y)_{\text{Sun}}$.

Additional information about the origin and Galactic evolution of carbon and oxygen may be obtained from differences in $[C/Fe]$, $[O/Fe]$, and $[C/O]$ between stellar populations. Precise abundance studies of F and G main-sequence stars in the solar neighborhood have revealed a clear difference in $[O/Fe]$ between thin- and thick-disk stars in the metallicity range $-0.7 < [Fe/H] < -0.2$ (Bensby et al. 2004, Ramírez et al. 2013). A similar difference in $[O/Fe]$ between the two populations of high- and low- α^2 halo stars identified by Nissen & Schuster (2010) has been found by Ramírez et al. (2012). In the case of carbon, Reddy et al. (2006) have found evidence of a systematic difference in $[C/Fe]$ between thin- and thick-disk stars, but this is not confirmed by Bensby & Feltzing (2006). For the high- and low- α halo stars, Nissen & Schuster (2014) found indications of a systematic difference in $[C/Fe]$, but this should be studied further.

More metal-rich stars, i.e., those having $[Fe/H] > -0.2$, also seem to have a bimodal distribution of various abundance ratios. The precise abundances of 1111 F and G stars in the solar neighborhood based on HARPS spectra (Adibekyan et al. 2011, 2012) have revealed the existence of a population of metal-rich, α -element-enhanced stars having $[\alpha/Fe] \simeq +0.1$ in contrast to normal thin-disk stars with $[\alpha/Fe] \simeq +0.0$. Bensby et al. (2014) confirm the existence of these α -enhanced stars, but consider them to belong to the thick-disk population. Haywood et al. (2013) also consider the metal-rich, α -enhanced stars to belong to the thick-disk sequence in the $[\alpha/Fe] - [Fe/H]$ diagram. They have determined precise ages for the upper main-sequence HARPS stars and find the thick-disk stars to have a well-defined age-metallicity relation ranging from 13 Gyr at $[Fe/H] \simeq -1$ to 8 Gyr at $[Fe/H] \simeq +0.2$. In contrast, thin-disk stars with $[Fe/H] > -0.2$ have ages less than 8 Gyr and a poorly defined age-metallicity relation.

The analysis of HARPS stars by Adibekyan et al. (2012) does not include C and O abundances. Hence, it remains to be seen if the two disk populations can be traced in $[C/Fe]$ and $[O/Fe]$ at metallicities up to $[Fe/H] \simeq +0.2$. The abundances of C and O are furthermore of great interest in connection with exoplanets. In some recent studies with carbon abundances derived from high-excitation C I lines and oxygen abundances from the $\lambda 6300$ [O I] line (Delgado Mena et al. 2010; Petigura & Marcy 2011) the carbon-to-oxygen ratio ³, C/O , in metal-rich F and G stars has been found to range from ~ 0.4 to $\gtrsim 1.0$, i.e., up to a factor of two higher than the solar ratio, $C/O_{\odot} \simeq 0.55$ (Asplund et al. 2009; Caffau et al. 2008, 2010). This has led to suggestions about the existence of exo-planets consisting of carbides and graphite instead of Earth-like silicates (Kuchner & Seager 2005; Bond et al. 2010). However, an alternative study by Nissen (2013) with oxygen abundances determined from the $\lambda 7774$ O I triplet results in a tight, slightly increasing relation between C/O and $[Fe/H]$ corresponding to $C/O \simeq 0.8$ at the highest metallicities ($[Fe/H] = +0.4$). This result is supported by a recent study of Teske et al. (2014) of C/O ratios in 16 stars with transiting planets. Furthermore, the very low frequency ($< 10^{-3}$) of carbon stars among K and M dwarf suggests that $C/O > 1$ is also very rare among solar-type stars (Fortney 2012). Still, there is need for further studies of C/O ratios in stars hosting planets.

² α refers to the average abundance of the α -capture elements, Mg, Si, Ca, and Ti.

³ C/O is defined as N_C/N_O , where N_C and N_O are the number densities of carbon and oxygen nuclei, respectively. It should not be confused with the solar-normalized logarithmic ratio, $[C/O]$

There may be other effects in addition to chemical evolution and population differences, which cause carbon and oxygen abundances to vary among F and G stars. In a very precise comparison of abundances in the Sun and 11 solar twin stars, Meléndez et al. (2009) found the Sun to have a $\sim 20\%$ depletion of refractory elements like Fe relative to volatile elements like C and O. They suggest that this may be related to depletion of refractory elements when terrestrial planets formed. Their results are supported by Ramírez et al. (2014), who in a strictly differential abundance analysis for groups of stars with similar T_{eff} , $\log g$, and $[Fe/H]$ values find the slope of $[X/Fe]$ versus condensation temperature T_C of element X to vary with an amplitude of $\sim 10^{-4}$ dex K^{-1} corresponding to variations of ~ 0.1 dex in $[C/Fe]$ and $[O/Fe]$. Based on HARPS spectra, González Hernández et al. (2010, 2013) find, however, smaller variations of the slope of $[X/Fe]$ versus T_C and both positive and negative slopes for ten stars with detected super-Earth planets, which casts doubts about the suggestion that a high volatile-to-refractory element ratio can be used as a signature of terrestrial planets. Clearly, more work is needed to explain the small variations in the volatile-to-refractory element ratio and to confirm that such variations really occur.

In this paper we address some of the problems mentioned above by determining precise C and O abundances for two samples of F and G stars, i.e., 66 disk stars with HARPS and FEROS spectra, and 85 halo and thick-disk stars from Nissen & Schuster (2010). We aim at getting new information on the evolution of $[C/Fe]$, $[O/Fe]$, and $[C/O]$ in stellar populations and to determine C/O ratios for stars with and without detected planets.

2. Stellar spectra and equivalent widths

2.1. The HARPS-FEROS sample of disk stars

Based on Adibekyan et al. (2012) we have selected 66 main-sequence stars with $5400 \text{ K} < T_{\text{eff}} < 6400 \text{ K}$, which have high signal-to-noise (S/N) HARPS and FEROS spectra available in the ESO Science Archive. This sample includes 32 stars with detected planets from Nissen (2013), and 34 new stars many of which have no detected planets. Except for HD 203608 with $[Fe/H] = -0.66$, the stars have metallicities in the range $-0.5 < [Fe/H] < +0.5$, and most of them are thin-disk stars, but a few have thick-disk kinematics.

The HARPS spectra cover a wavelength range from 3800 to 6900 Å with a resolution of $R \simeq 115\,000$ (Mayor et al. 2003). After combination of many individual spectra of a given star, the S/N exceeds 300 for most of the stars. These spectra were used to measure the equivalent widths (EWs) of the $\lambda\lambda 5052, 5380$ C I lines and the forbidden [OI] line at 6300 Å, if not disturbed by telluric O₂ lines. In addition, the EWs of 12 Fe II lines listed in Table 1 were measured from the HARPS spectra.

The FEROS (Kaufer et al. 1999) spectra, which have a resolution of $R \simeq 48\,000$ and a typical S/N of 200, were used to measure the EWs of the O I triplet lines at 7774 Å.

As described in Nissen (2013), the spectra were first normalized with the IRAF continuum task using a low order cubic spline fitting function. Then the IRAF plot task was used to measure equivalent widths by Gaussian fitting relative to local continuum regions selected to be free of lines in the solar spectrum. Care was taken to use the same continuum windows in all stars.

References for the stellar spectra, S/N ratios, and measured EW values are given in Table 2. In addition, we have used HARPS and FEROS spectra of reflected sunlight from Ceres

Table 1. Line data and derived solar abundances.

ID	Wavelength (Å)	χ_{exc} (eV)	$\log(gf)$	EW_{\odot} (mÅ)	$A(X)_{\odot}^a$ LTE	$A(X)_{\odot}$ non-LTE
C I	5052.17	7.685	-1.301	35.9	8.44	8.43
C I	5380.34	7.685	-1.616	21.5	8.44	8.43
[O I]	6300.31	0.000	-9.720	3.7 ^b	8.68	
O I	7771.94	9.146	0.369	71.8	8.88	8.66
O I	7774.17	9.146	0.223	61.8	8.86	8.66
O I	7775.39	9.146	0.002	48.6	8.84	8.67
Fe II	5414.08	3.22	-3.580	28.1	7.47	
Fe II	5425.26	3.20	-3.220	42.0	7.43	
Fe II	5991.38	3.15	-3.540	31.2	7.43	
Fe II	6084.11	3.20	-3.790	21.0	7.45	
Fe II	6113.33	3.22	-4.140	11.6	7.47	
Fe II	6149.25	3.89	-2.690	36.3	7.40	
Fe II	6238.39	3.89	-2.600	44.3	7.51	
Fe II	6239.95	3.89	-3.410	12.7	7.41	
Fe II	6247.56	3.89	-2.300	52.7	7.40	
Fe II	6369.46	2.89	-4.110	19.8	7.43	
Fe II	6432.68	2.89	-3.570	41.3	7.45	
Fe II	6456.39	3.90	-2.050	63.2	7.39	

Notes. ^(a) For an element X, $A(X) \equiv \log(N_X/N_H) + 12.0$.

^(b) This value refers to the EW of the [O I] line after correction for the Ni I contribution to the [O I]-Ni I $\lambda 6300$ blend. The total EW of the blend is 5.4 mÅ.

and Ganymede to represent the solar-flux spectrum. The combined HARPS spectrum has $S/N \approx 600$ and the FEROS solar-flux spectrum has $S/N \approx 400$ in the O I-triplet region. The measured EWs are given in Table 1 and are used in a differential model-atmosphere analysis of the stars with respect to the Sun.

2.2. The UVES-FIES sample of halo and thick-disk stars

The second sample, for which we have determined C and O abundances, consists of high-velocity, F and G main-sequence stars in the solar neighborhood from Nissen & Schuster (2010). These stars have metallicities in the range $-1.6 < [\text{Fe}/\text{H}] < -0.4$ and most of them belong to the halo population, i.e. they have space velocities with respect to the local standard of rest (LSR) larger than 180 km s^{-1} , but 16 stars with thick-disk kinematics are included. Spectra of stars on the southern sky were acquired from the VLT/UVES archive. They have resolutions $R \approx 55\,000$ and S/N ratios from 250 to 500. Northern stars were observed with the FIES spectrograph at the Nordic Optical Telescope at a resolution of $R \approx 40\,000$ and with $S/N \approx 140 - 200$. Further details are given in Nissen & Schuster (2010, Tables 1 and 2).

The UVES and FIES spectra include the C I lines at 5052 and 5380 Å, but the O I triplet at 7774 Å is not covered. Instead, we have obtained equivalent widths for the O I lines from other sources, first of all Ramírez et al. (2012), who measured EWs for the majority of the Nissen-Schuster stars based on high resolution spectra observed with the HET/HRS, Keck/HIRES, and Magellan/MIKE spectrographs. In addition, we have included EW-values from Nissen & Schuster (1997) for 15 stars with ESO NTT/EMMI spectra, and from Nissen et al. (2002) for six stars with UVES image slicer spectra. Finally, new EW measurements were carried out for two stars that have FEROS spectra available. Table 3 lists the results with mean values given, if there is more than one source for a star.

As a check of the accuracy of the equivalent width measurements for the O I triplet, Fig. 1 shows a comparison of values

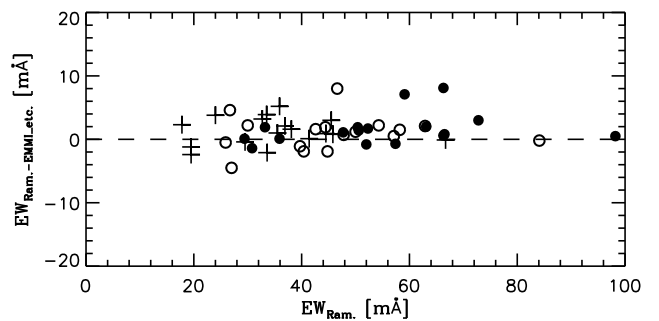


Fig. 1. Comparison of O I equivalent widths from Ramírez et al. (2012) and values based on EMMI, UVES and FEROS spectra. Filled circles refer to O I $\lambda 7771.9$, open circles to O I $\lambda 7774.2$, and crosses to O I $\lambda 7775.4$.

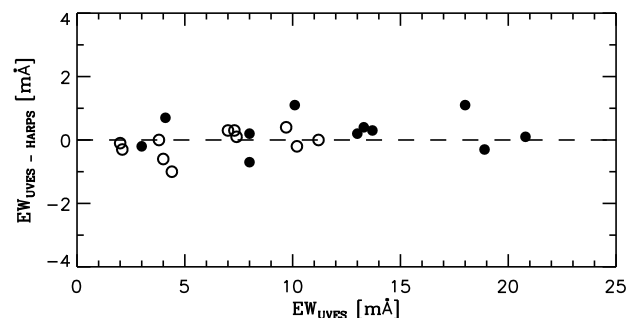


Fig. 2. Comparison of C I equivalent widths measured from UVES and HARPS spectra, respectively. Filled circles refer to C I $\lambda 5052.2$ and open circles to C I $\lambda 5380.3$.

from Ramírez et al. (2012) and the other sources mentioned (EMMI, UVES, and FEROS). As seen the agreement is quite satisfactory. There is a mean difference of 1.3 mÅ (Ramírez – other) with an rms scatter of 2.4 mÅ.

For 11 stars with UVES spectra, HARPS spectra are also available. Fig. 2 shows a comparison of the EWs of the C I $\lambda 5052, 5380$ lines measured with the two instruments. As seen, there is an excellent agreement with a mean difference (UVES – HARPS) of 0.1 mÅ and a rms deviation of only 0.5 mÅ. This good agreement can be ascribed to the high resolution and S/N of the two sets of spectra. The FIES spectra have lower resolution and S/N resulting in more uncertain EW measurements for the C I lines with errors on the order of 2 mÅ.

The weak [O I]-Ni I blend could be measured in UVES spectra of 13 of the most metal-rich halo and thick-disk stars. Five of these stars also have HARPS spectra. The mean difference of the two sets of EWs is 0.0 mÅ and the rms deviation is 0.4 mÅ.

To illustrate the high quality of the spectra applied, we show in Fig. 3 a region around the $\lambda 5052$ C I line for a low-alpha star, HD 105004, and a high-alpha star, G 05-40, with similar atmospheric parameters and metallicities. As seen, the Fe I lines have the same strengths in the two stars, but the C I line (and a Ti I line) is weaker in the low-alpha star.

3. Model-atmosphere analysis and non-LTE corrections

Plane parallel (1D) model atmospheres interpolated to the T_{eff} , $\log g$, $[\text{Fe}/\text{H}]$, and $[\alpha/\text{Fe}]$ values of the stars were obtained from the MARCS grid (Gustafsson et al. 2008) and the Uppsala pro-

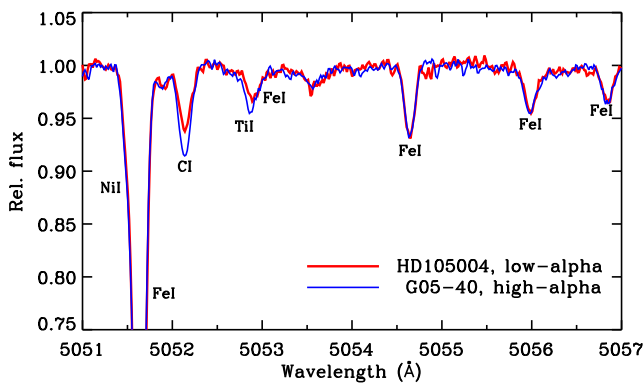


Fig. 3. UVES spectra around the $\lambda 5052$ C I line for the low-alpha star, HD 105004 with parameters $(T_{\text{eff}}, \log g, [\text{Fe}/\text{H}], [\alpha/\text{Fe}]) = (5852 \text{ K}, 4.35, -0.83, 0.14)$, and the high-alpha star, G05-40 with $(T_{\text{eff}}, \log g, [\text{Fe}/\text{H}], [\alpha/\text{Fe}]) = (5892 \text{ K}, 4.20, -0.83, 0.31)$.

gram EQWIDTH was used to calculate equivalent widths as a function of element abundance assuming LTE. By interpolating to the observed EW, we then obtain the LTE abundance corresponding to a given line.

Line data used in the analysis are given in Table 1. The sources of gf -values are Hibbert et al. (1993) for C I lines, Hibbert et al. (1991) for O I lines, and Meléndez & Barbuy (2009) for Fe II lines. As the analysis is made differentially to the Sun line by line, possible errors in these gf -values cancel out. Doppler broadening due to microturbulence is specified by a depth-independent parameter, ξ_{turb} . Collisional broadening caused by neutral hydrogen and helium atoms is based on the Unsöld (1955) approximation with an enhancement factor of two for the C I lines, whereas quantum mechanical calculations of Barklem et al. (2000) and Barklem & Aspelund-Johansson (2005) is used for the O I and Fe II lines.

Non-LTE corrections calculated by Fabbian et al. (2009) were applied to the oxygen abundances derived from the O I triplet. Fabbian et al. use a model atom with 54 energy levels and adopt electron collision cross sections from Barklem (2007). Inelastic collisions with hydrogen atoms were described by the classical Drawin formula (Drawin 1968) scaled by an empirical factor S_{H} . Calculations were performed for both $S_{\text{H}} = 0$ and 1, which allow us to interpolate the non-LTE corrections to $S_{\text{H}} = 0.85$, i.e., the value preferred by Pereira et al. (2009) based on a study of the solar center-to-limb variation of the O I triplet lines.

As seen from Table 1, the solar non-LTE corrections range from -0.22 to -0.17 dex for the three O I lines. According to Fabbian et al. (2009), the corrections depend strongly on T_{eff} ; stars cooler than the Sun have less negative non-LTE corrections, and warmer stars have more negative corrections. This leads to very significant differential non-LTE corrections of $[\text{O}/\text{H}]$ for our sample of stars ranging from about -0.2 dex at $T_{\text{eff}} \approx 6300$ K to $+0.1$ dex at $T_{\text{eff}} \approx 5400$ K.

The non-LTE corrections for carbon abundances derived from the C I $\lambda\lambda 5052, 5380$ lines are much smaller than those for the O I triplet. In this paper we adopt the calculations of Takeda & Honda (2005), who assume $S_{\text{H}} = 1$. The corrections are -0.01 dex for the Sun and changes only slightly with T_{eff} and $\log g$.

Furthermore, we note that the Fe abundance determined from Fe II lines is unaffected by departures from LTE (e.g., Mashonkina et al. 2011; Lind et al. 2012). This is also the case for oxygen abundances derived from the forbidden [O I] line at

6300 Å (e.g. Kiselman 1993). This line is, however, affected by a Ni I blend as further discussed in Sect. 5.

4. Stellar parameters

4.1. The HARPS-FEROS sample

For these stars, Adibekyan et al. (2012) have given effective temperatures, T_{eff} , and surface gravities, $\log g$. The values were originally derived from the HARPS spectra by Sousa et al. (2008, 2011a, 2011b) by requesting that $[\text{Fe}/\text{H}]$ should not have any systematic dependence on excitation potential of the lines and that the same iron abundance is obtained from Fe I and Fe II lines.

As an alternative, we have determined photometric parameters for the HARPS-FEROS sample of disk stars. T_{eff} is derived from the $(b-y)$ and $(V-K)$ color indices using the calibrations of Casagrande et al. (2010), which are based on T_{eff} values determined with the infrared flux method (IRFM). V magnitudes and $(b-y)$ were taken from Olsen (1983) and K magnitudes from the 2MASS catalogue (Skrutskie et al. 2006). For nine stars, the 2MASS K value is uncertain due to saturation. In these cases, T_{eff} has been determined from $(b-y)$ alone. Otherwise we have adopted the mean T_{eff} derived from $(b-y)$ and $(V-K)$.

The surface gravity was determined from the relation

$$\log \frac{g}{g_{\odot}} = \log \frac{M}{M_{\odot}} + 4 \log \frac{T_{\text{eff}}}{T_{\text{eff},\odot}} + 0.4(M_{\text{bol}} - M_{\text{bol},\odot}), \quad (1)$$

where M is the mass of the star and M_{bol} the absolute bolometric magnitude. Hipparcos parallaxes (van Leeuwen 2007) are used to derive M_{V} . Bolometric corrections were adopted from Casagrande et al. (2010), and stellar masses were obtained by interpolating in the luminosity - $\log T_{\text{eff}}$ diagram between the Yonsei - Yale evolutionary tracks of Yi et al. (2003); see Nissen & Schuster (2012) for details.

Metallicities were determined from the twelve Fe II lines listed in Table 1. These lines have equivalent widths spanning a range that allows us to determine the microturbulence parameter, ξ_{turb} , from the requirement that the derived $[\text{Fe}/\text{H}]$ should not depend on EW . The analysis is made differentially with respect to the Sun adopting a solar microturbulence of 1.0 km s^{-1} .

This procedure of determining stellar parameters has to be iterated until consistency, because the T_{eff} calibrations, bolometric corrections and mass determinations depend on $[\text{Fe}/\text{H}]$.

All stars have distances less than 60 pc according to their Hipparcos parallaxes. We may therefore assume that the observed $(b-y)$ and $(V-K)$ indices and hence T_{eff} are not affected by interstellar reddening.

The rms dispersion of the difference of T_{eff} determined from $(b-y)$ and $(V-K)$, respectively, is 62 K. From this we estimate that the mean photometric temperature, $T_{\text{eff}}(\text{phot}) = 1/2 \times (T_{\text{eff}}(b-y) + T_{\text{eff}}(V-K))$ is determined with an internal one-sigma error of ~ 30 K. At a given metallicity, this high precision is confirmed by comparing the photometric T_{eff} values with the spectroscopic temperatures of Adibekyan et al. (2012), who also quote an error of 30 K; the rms scatter of $\Delta T_{\text{eff}} = T_{\text{eff}}(\text{phot}) - T_{\text{eff}}(\text{spec})$ in metallicity intervals of 0.2 dex is about 40 K. As seen from Fig. 4, there is, however, a systematic trend of ΔT_{eff} as a function of metallicity. The difference between the two sets of temperatures decreases from about $+50$ K at $[\text{Fe}/\text{H}] = -0.4$ to about -60 K at $[\text{Fe}/\text{H}] = +0.4$.

Because of the small error in the Hipparcos parallaxes, the estimated error in $\log g$ (HIP) is about 0.05 dex. This small statistical error is supported by the comparison of photometric and spectroscopic gravities shown in Fig. 5; the rms scatter of

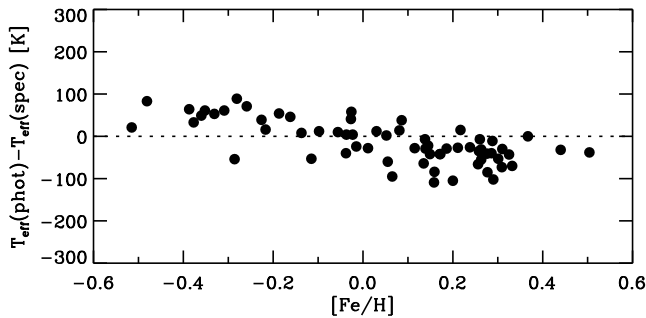


Fig. 4. Comparison of photometric temperatures for the HARPS-FEROS stars derived in this paper and the spectroscopic temperatures derived by Sousa et al. (2008, 2011a, 2011b)

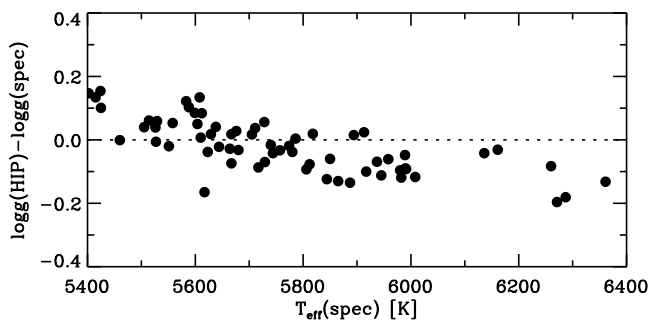


Fig. 5. Comparison of surface gravities for the HARPS-FEROS stars derived via Hipparcos parallaxes in this paper and the spectroscopic gravities derived by Sousa et al. (2008, 2011a, 2011b).

$\Delta \log g = \log g(\text{HIP}) - \log g(\text{spec})$ in T_{eff} intervals of 200 K is only 0.06 dex, but there is a trend of $\Delta \log g$ as a function of T_{eff} ranging from about +0.1 dex at $T_{\text{eff}} = 5400$ K to about -0.15 dex at the highest temperatures. This trend is not easily explained; according to Lind et al. (2012) non-LTE effects on the ionization balance of Fe (used to determine the spectroscopic gravities) are almost negligible for the effective temperatures, gravities and metallicities of the present HARPS-FEROS sample of stars. The same problem is discussed by Bensby et al. (2014), who note that dwarf stars with spectroscopic gravities have a flat distribution of $\log g$ as a function of T_{eff} . In contrast, gravities derived from Hipparcos parallaxes show an increasing trend of $\log g$ when T_{eff} decreases from 6500 K to 5000 K in agreement with predictions from isochrones. Hence, it looks like the Hipparcos gravities are more reliable, but it is puzzling why the spectroscopic gravities have systematic errors. As discussed by Bensby et al. (2014), the small departures from LTE for the Fe I lines predicted with 1D models (Lind et al. 2012) cannot explain the problem. Perhaps one may be able to solve the problem when full 3D, non-LTE calculations of the ionization balance of Fe becomes available.

In view of the problems with the spectroscopic gravities, we prefer to apply the photometric values based on Hipparcos parallaxes. For consistency we then also adopt the photometric T_{eff} values based on the $(b-y)$ and $(V-K)$ colors and the Casagrande et al. (2010) calibration. These parameters are given in Table 4 together with the derived values of $[\text{Fe}/\text{H}]$ and ξ_{turb} , which agree well with those of Adibekyan et al. (2012) despite of the differences in T_{eff} and $\log g$. Mean differences (this paper – Adibekyan) and rms scatters are: $\Delta [\text{Fe}/\text{H}] = 0.015 \pm 0.04$ and $\Delta \xi_{\text{turb}} = 0.03 \pm 0.09 \text{ km s}^{-1}$.

4.2. The UVES-FIES sample

This sample consists of halo and thick-disk stars with distances up to 350 pc, which means that interstellar reddening may affect the effective temperature determined from color indices and that in most cases the Hipparcos parallax has a too large error to be used to determine the surface gravity. Hence, it is not possible to determine precise photometric values of T_{eff} and $\log g$. Instead, we have followed the method applied by Nissen & Schuster (2010, 2011), who first determined T_{eff} and $\log g$ for two nearby, unreddened thick-disk stars, HD 22879 and HD 76932, with the photometric method described in the previous section. These standard stars are analyzed relative to the Sun using lines having EWs less than about 100 mÅ in the solar spectrum. An inverted abundance analysis then yields gf -values for the full set of lines given in Nissen & Schuster (2011, Table 3). Using these gf -values, a model atmosphere analysis makes it possible to determine spectroscopic values of T_{eff} and $\log g$ as well as high-precision abundances relative to the standard stars.

In Nissen & Schuster (2010, 2011), the calibrations of Ramírez & Meléndez (2005) were used to determine T_{eff} of the standard stars. The more accurate calibrations by Casagrande et al. (2010) show, however, a systematic offset of about +100 K in T_{eff} relative to the Ramírez & Meléndez values. We have, therefore, increased the T_{eff} values of the standard stars by 100 K, and repeated the spectroscopic analysis of the other stars, i.e., determined T_{eff} from the excitation balance of weak ($EW < 50 \text{ mÅ}$) Fe I lines, $\log g$ from the Fe I/Fe II ionization balance, and ξ_{turb} by requesting that the derived $[\text{Fe}/\text{H}]$ has no systematic dependence on EW for Fe I lines. The updated parameters are given in Table 5 for 85 stars for which C and/or O abundances have been determined⁴. Relative to the parameter values given in Nissen & Schuster (2010, 2011), there are small changes in $\log g$ ranging from +0.03 dex for the standard stars to about +0.08 dex for the coolest stars. $[\text{Fe}/\text{H}]$ is decreased by approximately 0.02 dex for all stars, whereas $[\alpha/\text{Fe}]$ is practically the same, i.e., changes are within ± 0.005 dex.

As a check of the spectroscopic values of T_{eff} , we have compared with IRFM values from Casagrande et al. (2010) for a subsample of 41 stars in common. As seen from Fig. 6, there is no significant trend of $\Delta T_{\text{eff}} = T_{\text{eff}}(\text{spec}) - T_{\text{eff}}(\text{IRFM})$ as a function of $[\text{Fe}/\text{H}]$, nor is there any trend of ΔT_{eff} with T_{eff} . The mean value of ΔT_{eff} is -10 K with an rms scatter of ± 70 K. The largest contribution to this scatter arises from the error in $T_{\text{eff}}(\text{IRFM})$, which is on the order of ± 60 K. These numbers suggest that the error in $T_{\text{eff}}(\text{spec})$ is on the order of ± 35 K.

The spectroscopic gravities have been tested by comparing with gravities based on Hipparcos parallaxes for 24 stars⁵, which have no detectable interstellar NaD lines (indicating that interstellar reddening is negligible) and parallaxes with an error of less than 10%. As seen from Fig. 7, there is a satisfactory agreement between the two sets of gravities although one star, CD -33 3337, shows a large deviation. If this outlier is excluded, the mean of $\Delta \log g = \log g(\text{HIP}) - \log g(\text{spec})$ is 0.03 dex with an rms scatter of ± 0.085 dex. With an estimated average error of ± 0.06 dex for $\log g(\text{HIP})$, the error of $\log g(\text{spec})$ becomes ± 0.06 dex. If CD -33 3337 is included, the scatter of $\Delta \log g$ raises to ± 0.10 dex and the error of $\log g(\text{spec})$ to ± 0.08 dex.

⁴ The C and s -process rich CH-subgiant, G 24-25 (Liu et al. 2012) is not included.

⁵ The two standard stars are not included in this comparison, because their spectroscopic and photometric gravities agree by definition.

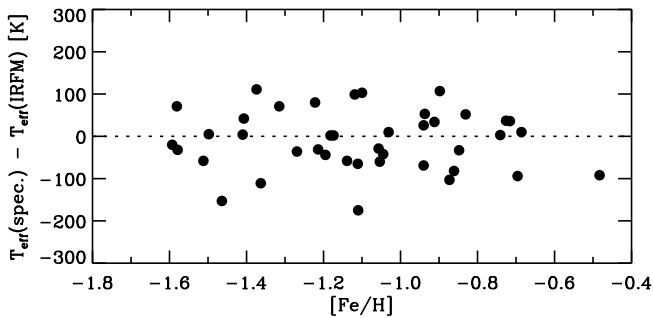


Fig. 6. Comparison of spectroscopic temperatures derived in this paper for the UVES-FIES sample and temperatures determined by Casagrande et al. (2010) with the IRFM method.

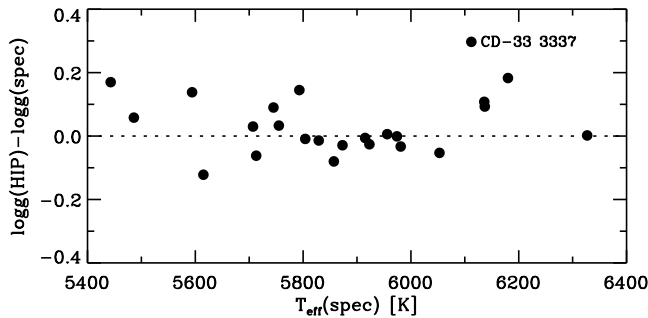


Fig. 7. Comparison of photometric gravities derived via Hipparcos parallaxes and spectroscopic gravities derived from Fe I and Fe II lines for a subsample of the UVES-FIES stars having parallax errors less than 10% .

Interestingly, there is no indication of a trend of $\Delta \log g$ as a function of T_{eff} like the trend seen in Fig. 4 for the more metal-rich disk stars. Thus, it seems that we can use spectroscopic values of $\log g$ for the FIES – UVES sample of halo and thick-disk stars without worrying about systematic errors as a function of T_{eff} .

5. Carbon and Oxygen abundances

The derived LTE and non-LTE values of $[\text{C}/\text{H}]$ and $[\text{O}/\text{H}]$ are given in Tables 4 and 5. In the case of $[\text{O}/\text{H}]$ we list both the value derived from the O I triplet and the value based on the [O I] $\lambda 6300$ line, if measured. Most of the disk stars have $[\text{O}/\text{H}]_{6300}$ available, whereas the [O I] line is too weak for the majority of halo stars to be detectable.

5.1. Statistical errors

Statistical errors of the various abundance ratios have been determined for two representative stars: a disk star, HD 196050, with $[\text{Fe}/\text{H}] = +0.26$ and a metal-poor star from the UVES-FIES sample, HD 199289, with $[\text{Fe}/\text{H}] = -1.05$. As seen from Tables 6 and 7, $[\text{O}/\text{H}]_{6300}$ derived from the [O I] $\lambda 6300$ line is only slightly affected by the uncertainty in T_{eff} , whereas $[\text{O}/\text{H}]_{7774}$ derived from the O I triplet lines is sensitive to the error in T_{eff} . $[\text{Fe}/\text{H}]$, $[\text{C}/\text{H}]$, and $[\text{O}/\text{H}]$ are all significantly affected by the error in $\log g$, but this dependence cancels out for $[\text{C}/\text{Fe}]$, $[\text{O}/\text{Fe}]$, and $[\text{C}/\text{O}]$. Furthermore, we note that the errors in $[\text{Fe}/\text{H}]$ and ξ_{turb} are of minor importance for the derived abundance ratios.

The errors of $[\text{Fe}/\text{H}]$, $[\text{C}/\text{H}]$, and $[\text{O}/\text{H}]_{7774}$ arising from the uncertainty of the measured equivalent widths have been esti-

mated from the line-to-line scatter of the derived abundances. In the case of $[\text{O}/\text{H}]_{6300}$, the EW-error corresponds to an uncertainty of the equivalent width of the $\lambda 6300$ [O I] line of ± 0.4 mÅ as estimated in Sect. 2.1.

The total errors listed in the last rows of Tables 6 and 7 are calculated by adding the individual errors in quadrature. The small estimated error of $[\text{C}/\text{Fe}]$ (± 0.028 dex) in Table 6 is due to the extremely high S/N of the HARPS spectra, and the small sensitivity of $[\text{C}/\text{Fe}]$ to uncertainties in the atmospheric parameters. For the UVES-FIES sample the error of $[\text{C}/\text{Fe}]$ is larger, because of the weakness of the C I lines, especially in spectra of metal-poor halo stars belonging to the low-alpha population. In some of the figures in Sect. 6, data will be shown with individual error bars.

5.2. Systematic errors; the $[\text{O}/\text{H}]_{7774} - [\text{O}/\text{H}]_{6300}$ discrepancy.

In addition to statistical errors, we have to consider possible systematic errors of the abundances, especially in the case of oxygen abundances derived from the O I $\lambda 7774$ lines, because of the large non-LTE corrections and high sensitivity to T_{eff} . In order to reveal any problems, we have therefore compared oxygen abundances derived from the O I triplet with O abundances resulting from the forbidden oxygen line at 6300 Å.

As discussed in detail by Allende-Prieto et al. (2001), the absorption feature at 6300.3 Å is a blend of the [O I] line and a Ni I line, which makes it slightly asymmetric. From the best fit of the blend with profiles calculated from a 3D model atmosphere of the Sun, they derived a solar oxygen abundance of $A(\text{O})_{\odot} = 8.69$. Later, Johansson et al. (2003) measured an experimental oscillator strength of the Ni I line, $\log gf = -2.11 \pm 0.05$. When using this value and a solar nickel abundance of $A(\text{Ni})_{\odot} = 6.17$ (determined from 17 weak Ni I lines), Scott et al. (2009) obtained $A(\text{O})_{\odot} = 8.69$ from a 3D analysis. Repeating the analysis of the Ni I lines with a 1D MARCS model of the Sun, we obtain a Ni abundance of 6.15 and predict an equivalent width of 1.7 mÅ for the Ni I line in the $\lambda 6300$ blend. After subtracting this value from the measured EW of the [O I] - Ni I blend (5.4 mÅ) in the solar flux spectrum, a solar oxygen abundance of 8.68 is obtained, which agrees well with the 3D value.

For the stars we have first calculated the EW of the blending Ni I line using Ni abundances corresponding to the $[\text{Ni}/\text{Fe}]$ values of Adibekyan et al. (2012) for the HARPS-FEROS sample and those of Nissen & Schuster (2010) for the UVES-FIES sample. The measured EW of the [O I] - Ni I blend is then corrected for the contribution from the Ni I line before the oxygen abundance is determined.

A comparison of non-LTE oxygen abundances derived from the O I-triplet and O abundances from the [O I] line is shown in Fig. 8. The average of $\Delta[\text{O}/\text{H}] = [\text{O}/\text{H}]_{7774} - [\text{O}/\text{H}]_{6300}$ is 0.010 dex with an rms scatter of ± 0.07 dex, which corresponds well to the errors estimated in Tables 6 and 7. As seen, there is, however, a systematic deviation for the coolest and most metal-rich stars on the order of $\Delta[\text{O}/\text{H}] \sim +0.10$, i.e., the triplet provides higher oxygen abundances than the [O I] $\lambda 6300$ line. A similar deviation was found by Teske et al. (2013) for the planet hosting star 55 Cnc having $T_{\text{eff}} = 5350$ K, $\log g = 4.44$, and $[\text{Fe}/\text{H}] = +0.34$. They obtained $[\text{O}/\text{H}]_{7774} \approx 0.22$ to 0.27 (depending on which non-LTE corrections were adopted) and $[\text{O}/\text{H}]_{6300} \approx 0.08$.

There are several possible explanations of the discrepancy between $[\text{O}/\text{H}]$ derived from the O I triplet and the [O I] $\lambda 6300$ line. Given that $[\text{Ni}/\text{Fe}]$ increases slightly and $[\text{O}/\text{Fe}]$ decreases

Table 6. Errors in abundance ratios of the metal-rich star HD 196050^a caused by errors in model atmosphere parameters and equivalent widths.

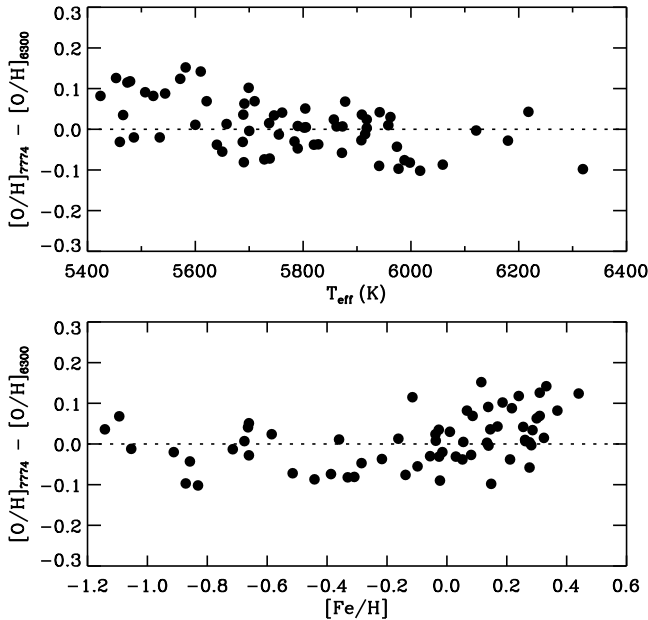
	$\sigma[\text{Fe}/\text{H}]$	$\sigma[\text{C}/\text{H}]$	$\sigma[\text{O}/\text{H}]_{6300}^b$	$\sigma[\text{O}/\text{H}]_{7774}^c$	$\sigma[\text{C}/\text{Fe}]$	$\sigma[\text{O}/\text{Fe}]_{6300}^b$	$\sigma[\text{O}/\text{Fe}]_{7774}^c$	$\sigma[\text{C}/\text{O}]_{7774}^c$
$\sigma(T_{\text{eff}}) = \pm 30 \text{ K}$	∓ 0.011	∓ 0.020	± 0.002	∓ 0.035	∓ 0.009	± 0.013	∓ 0.024	± 0.015
$\sigma(\log g) = \pm 0.05 \text{ dex}$	± 0.020	± 0.017	± 0.023	± 0.021	∓ 0.003	± 0.003	± 0.001	∓ 0.004
$\sigma[\text{Fe}/\text{H}] = \pm 0.03 \text{ dex}$	± 0.008	± 0.000	± 0.010	± 0.001	∓ 0.008	± 0.002	∓ 0.007	∓ 0.001
$\sigma(\xi_{\text{turb}}) = \pm 0.06 \text{ km s}^{-1}$	∓ 0.014	∓ 0.003	± 0.000	∓ 0.005	± 0.011	± 0.014	± 0.009	± 0.002
$\sigma(EW)$	± 0.010	± 0.020	± 0.040	± 0.025	± 0.022	± 0.041	± 0.027	± 0.032
$\sigma(\text{total})$	± 0.030	± 0.033	± 0.047	± 0.048	± 0.028	± 0.045	± 0.038	± 0.036

Notes. ^(a) ($T_{\text{eff}}, \log g, [\text{Fe}/\text{H}]$) = (5852 K, 4.22, +0.26) ^(b) The oxygen abundance is based on the [O I] $\lambda 6300$ line. ^(c) The oxygen abundance is based on the O I $\lambda 7774$ triplet.

Table 7. Errors in abundance ratios of the metal-poor star HD 199289^a caused by errors in model atmosphere parameters and equivalent widths.

	$\sigma[\text{Fe}/\text{H}]$	$\sigma[\text{C}/\text{H}]$	$\sigma[\text{O}/\text{H}]_{6300}^b$	$\sigma[\text{O}/\text{H}]_{7774}^c$	$\sigma[\text{C}/\text{Fe}]$	$\sigma[\text{O}/\text{Fe}]_{6300}^b$	$\sigma[\text{O}/\text{Fe}]_{7774}^c$	$\sigma[\text{C}/\text{O}]_{7774}^c$
$\sigma(T_{\text{eff}}) = \pm 35 \text{ K}$	∓ 0.002	∓ 0.018	± 0.012	∓ 0.034	∓ 0.016	± 0.014	∓ 0.032	± 0.016
$\sigma(\log g) = \pm 0.06 \text{ dex}$	± 0.022	± 0.024	± 0.024	± 0.023	± 0.002	± 0.002	± 0.001	± 0.001
$\sigma[\text{Fe}/\text{H}] = \pm 0.03 \text{ dex}$	± 0.002	∓ 0.002	± 0.004	∓ 0.001	∓ 0.004	± 0.002	∓ 0.003	∓ 0.001
$\sigma(\xi_{\text{turb}}) = \pm 0.06 \text{ km s}^{-1}$	∓ 0.008	± 0.000	± 0.000	∓ 0.003	± 0.008	± 0.008	± 0.005	± 0.003
$\sigma(EW)$	± 0.015	± 0.045	± 0.050	± 0.025	± 0.047	± 0.052	± 0.029	± 0.051
$\sigma(\text{total})$	± 0.028	± 0.054	± 0.057	± 0.048	± 0.050	± 0.055	± 0.044	± 0.054

Notes. ^(a) ($T_{\text{eff}}, \log g, [\text{Fe}/\text{H}]$) = (5915 K, 4.30, -1.05) ^(b) The oxygen abundance is based on the [O I] $\lambda 6300$ line. ^(c) The oxygen abundance is based on the O I $\lambda 7774$ triplet.


Fig. 8. Differences of non-LTE oxygen abundances derived from the O I $\lambda 7774$ triplet and oxygen abundances obtained from the [O I] $\lambda 6300$ line versus T_{eff} and $[\text{Fe}/\text{H}]$.

with increasing $[\text{Fe}/\text{H}]$, the Ni I line makes up a large fraction (up to 60%) of the [O I] - Ni I blend in spectra of metal-rich stars, whereas the corresponding fraction in the solar spectrum is $\sim 30\%$. These estimates are based on $\log gf = -2.11$ for the Ni I line as determined by Johansson et al. (2003). If $\log gf$ is

decreased by for example 0.15 dex, the importance of the Ni I line decreases, and the solar oxygen abundance derived from the [O I] $\lambda 6300$ line increases from $A(\text{O}) = 8.68$ to 8.74. For the cool, metal-rich stars in our sample the effect is even larger resulting in an increase in $[\text{O}/\text{H}]_{6300}$ of 0.05 dex to 0.10 dex, which removes most of the discrepancy seen in Fig. 8. A decrease in $\log gf$ of 0.15 dex is, however, three times larger than the error given by Johansson et al. (2003). A lower gf -value would, on the other hand, decrease the puzzling difference between oxygen abundances derived from the [O I] lines at 6300 and 6363 Å in spectra of dwarf stars (Caffau et al. 2013). Hence, we think that this possibility should be kept open.

One may ask if problems with the non-LTE corrections for the O I triplet could lead to too high [O/H] values compared to those derived from the [O I] $\lambda 6300$ line. The corrections of Fabbian et al. (2009) have a strong dependence of T_{eff} leading to *positive* corrections of [O/H] for dwarf stars cooler than the Sun. If no corrections are applied, i.e., LTE is assumed, the discrepancy shown in Fig. 8 for the cool, metal-rich stars in fact disappears, but instead there is a clear discrepancy for stars with $T_{\text{eff}} > 6000 \text{ K}$, and the scatter of $[\text{O}/\text{H}]_{7774} - [\text{O}/\text{H}]_{6300}$ increases from 0.07 dex to 0.09 dex. So, this is not a viable solution. There may, however, be other ways to solve the problem. Schuler et al. (2004, 2006) found that oxygen abundances derived from the O I triplet show a strong rise with decreasing effective temperature for dwarf stars having $T_{\text{eff}} < 5450 \text{ K}$ in the Pleiades and Hyades open clusters. At $T_{\text{eff}} = 5000 \text{ K}$ there is an overabundance of ~ 0.25 dex relative to the oxygen abundance in the range $5450 \text{ K} < T_{\text{eff}} < 6100 \text{ K}$, and at $T_{\text{eff}} = 4500 \text{ K}$ the overabundance has increased to ~ 0.75 dex. Schuler et al. (2006) suggest that this may be related to the presence of hot and cool spots on the stellar surface with the hot spots making a relative large contribution to the

EWs of the O I triplet in the cool Pleiades and Hyades stars. This effect may play a role for the coolest stars in our sample by contributing to the overabundance of $[O/H]_{7774}$ relative to $[O/H]_{6300}$, although our stars are on average older and probably less active than the Pleiades and Hyades stars.

A difference in oxygen abundances derived from 3D model atmospheres and 1D models is another potential problem. As discussed by Nissen et al. (2002), 3D corrections are more important for the $[O I] \lambda 6300$ line than the O I triplet, because the $[O I]$ line is formed in the upper layers of the atmosphere, where 3D-effects have the largest impact on the temperature structure. The dependence of 3D corrections on T_{eff} is however small, only 0.03 dex for a T_{eff} -increase of 400 K (Nissen et al. 2002, Table 6) and goes in the wrong direction to diminish the discrepancy between $[O/H]_{7774}$ and $[O/H]_{6300}$ at low T_{eff} .

We conclude from this discussion that there is no obvious explanation of the $[O/H]_{7774} - [O/H]_{6300}$ discrepancy for the cool, metal-rich stars in our sample, and that the problem could be with both $[O/H]_{7774}$ and $[O/H]_{6300}$. In the following section we shall, therefore, discuss results based on both sets of oxygen abundances.

6. Results and discussion

In this section, we show how $[C/Fe]$, $[O/Fe]$, and $[C/O]$ change as a function of increasing metallicity, $[Fe/H]$, for the four populations of stars identified in the solar neighborhood, and discuss how these trends may be explained in terms of Galactic chemical evolution and differences in origin of the various populations. We also investigate, if there are any systematic differences in the abundance ratios between stars hosting planets and stars for which no planets have been detected, and if there is evidence of a cosmic scatter in $[C/Fe]$ and $[O/Fe]$ for solar analog stars corresponding to the variations in the volatile-to-refractory element ratio claimed in some recent works (e.g. Meléndez et al. 2009, Ramírez et al. 2014).

6.1. Populations

As seen from Tables 4 and 5, stars have been classified into four different populations. For the HARPS-FEROS sample, the $[\alpha/Fe]$ - $[Fe/H]$ diagram of Adibekyan et al. (2013) is used to divide stars into thin- and thick-disk populations depending on whether they lie below or above the dividing line shown in their Fig. 1. At $[Fe/H] < -0.2$, there is a gap in $[\alpha/Fe]$ between the two populations, so a chemical separation is more clear than a kinematical separation, because thin- and thick-disk stars have considerable overlap in the Galactic velocity components. For the more metal-rich stars with $[Fe/H] > -0.2$, there is no gap between the thin- and thick-disk sequences in the $[\alpha/Fe]$ - $[Fe/H]$ diagram, so the population classification is less clear. Haywood et al. (2013) have, however, shown that the metal-rich, alpha-enhanced stars are older than the metal-rich thin-disk stars and that they form a smooth extension of the age-metallicity relation for the metal-poor thick-disk stars (see Fig. 10 in Haywood et al. 2013).

Stars in the UVES-FIES sample were classified by Nissen & Schuster (2010). If the total space velocity with respect to the LSR is larger than 180 km s^{-1} , a star is considered to be a halo star. As shown in Fig. 1 of Nissen & Schuster (2010), these stars have a bimodal distribution in the $[\alpha/Fe]$ - $[Fe/H]$ diagram allowing a classification into high- and low-alpha halo stars. The two halo populations are also well separated in other

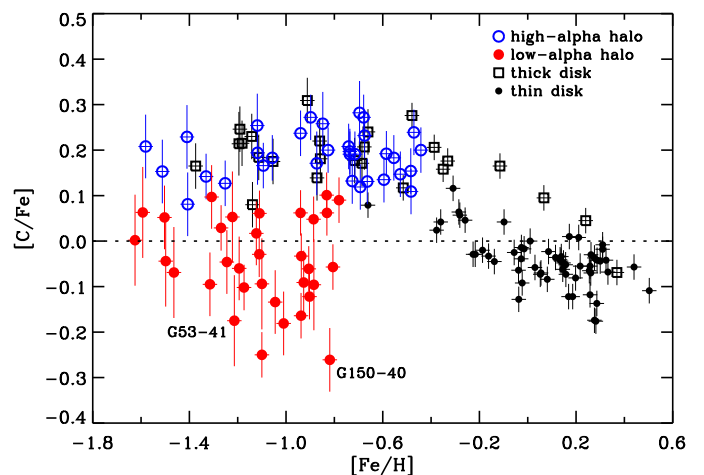


Fig. 9. $[C/Fe]$ versus $[Fe/H]$ for stars analyzed in this paper. The two Na-rich halo stars are marked.

abundance ratios such as Na/Fe and Ni/Fe with the low-alpha stars having abundances ratios similar to those of dwarf galaxies (Tolstoy et al. 2009). Furthermore, the two populations have different kinematical properties and ages, i.e., the low-alpha stars have larger space velocities and more negative (retrograde) V velocity components than the high-alpha stars, and they are on average younger by 2- 3 Gyr (Schuster et al. 2012). Altogether, this suggests that the low-alpha stars have been accreted from dwarf galaxies, whereas the high-alpha stars may have formed in situ during a dissipative collapse of proto-Galactic gas clouds.

The UVES-FIES sample includes 16 stars, which were classified by Nissen & Schuster (2010) as belonging to the thick disk based on their kinematics. All of these stars fall above the dividing line in the $[\alpha/Fe]$ - $[Fe/H]$ diagram of Adibekyan et al. (2013), so they would also be classified as thick-disk according to their chemical properties.

6.2. The $[C/Fe]$ and $[O/Fe]$ trends

The trends of $[C/Fe]$ and $[O/Fe]$ as a function of $[Fe/H]$ are shown in Figs. 9 and 10, respectively, with different symbols for the four populations discussed. In Fig. 10 we have applied the average oxygen abundance derived from the O I triplet and the $[O I] \lambda 6300$ line if both lines were measured. Individual error bars are given; they are relatively large in $[C/Fe]$ for the low-alpha halo stars due to the weakness of the C I lines.

As seen from Figs. 9 and 10, there are systematic differences between thin- and thick-disk stars. The group of thin-disk stars around $[Fe/H] \sim -0.3$ falls below the thick-disk sequence in both $[C/Fe]$ and $[O/Fe]$, and the thin-disk star HD 203608 at $[Fe/H] = -0.66$ also falls below. Furthermore, we note that the two metal-rich, alpha-enhanced stars with $[Fe/H]$ between -0.15 and $+0.15$ clearly fall above the thin-disk sequence, and lie on an extension of the more metal-poor thick-disk sequence. The third and the fourth metal-rich thick-disk stars with $[Fe/H]$ between $+0.2$ and $+0.4$ do not deviate significantly from the thin-disk stars suggesting that the two populations merge in $[C/Fe]$ and $[O/Fe]$ at the highest metallicities.

The high-alpha halo stars with $[Fe/H] < -0.8$ are distributed around a plateau of $[C/Fe] \approx 0.2$ in Fig. 9 and $[O/Fe] \approx 0.6$ in Fig. 10, whereas the low-alpha stars are shifted downwards with a decreasing trend as a function of increasing metallicity. In the case of $[O/Fe]$, this confirms the result of Ramírez

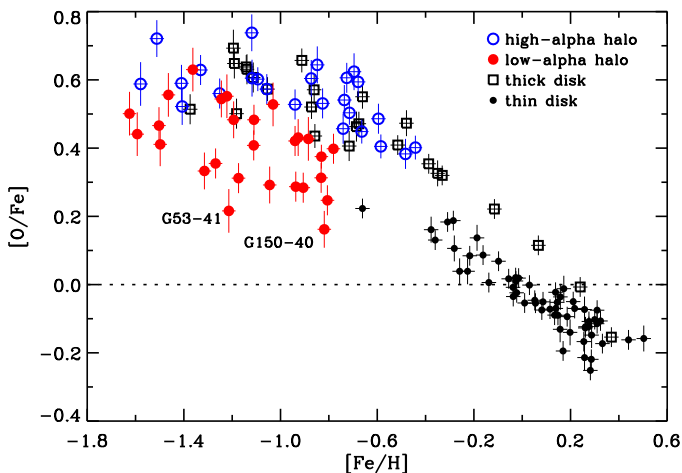


Fig. 10. $[O/Fe]$ versus $[Fe/H]$. For stars with both $[O/H]_{6300}$ and $[O/H]_{7774}$ available, the average oxygen abundance has been applied.

et al. (2012), although their $[O/Fe]$ values tend to be slightly lower. Furthermore, the trends of $[C/Fe]$ and $[O/Fe]$ resemble that of $[Mg/Fe]$ shown in Nissen & Schuster (2010) except for a constant offset; the high-alpha halo stars have a plateau at $[Mg/Fe] \approx 0.35$.

Figure 11 shows that $[C/Fe]$ and $[O/Fe]$ are well correlated and that the amplitude of the variations is about the same for the two abundance ratios, i.e., the data are well fitted with a line having a slope of one. Interestingly, the two stars with the lowest $[C/Fe]$ and $[O/Fe]$ values, G 53-41 and G 150-40, are Na-rich (Nissen & Schuster 2010). As discussed by Ramírez et al. (2012), they share the Na-O abundance anomaly of second generation stars born in globular clusters (Carretta et al. 2009).

The different trends of high- and low-alpha stars in Figs. 9 and 10 may be explained if the two populations were formed in systems with different star formation rates. According to this scenario, the high-alpha stars formed in regions with such a high star formation rate that mainly massive stars exploding as Type II SNe contributed to the chemical enrichment up to $[Fe/H] \approx -0.6$ at which metallicity Type Ia SNe started to contribute Fe causing $[O/Fe]$ to decrease. The low-alpha stars, on the other hand, originate in regions with a slow chemical evolution so that Type Ia SNe started to contribute iron at $[Fe/H] \approx -1.6$, or at an even lower metallicity. Bursts of star formation, as those shown in dwarf galaxies, could explain the low $[C/Fe]$ and $[O/Fe]$ present in low-alpha stars. These values are even lower, if Fe occurs between consecutive bursts (Carigi et al. 2002). The two Na-rich stars, G 53-41 and G 150-40, are exceptions as they have probably been formed in globular clusters as mentioned above.

As an alternative explanation of low-alpha halo stars, Kobayashi et al. (2014) suggest that they were formed in regions where the nucleosynthesis contribution of massive $M > 25M_{\odot}$ core collapse supernovae is missing due to stochastic variations of the IMF. These stochastic effects are more important in dwarf galaxies, due to the low content of available gas to form stars (Carigi & Hernandez 2008). This explanation is based on the yield calculations of Kobayashi et al. (2006) showing that the O/Fe and α/Fe ratio is significantly lower for 13 - 25 M_{\odot} supernovae than in the case of $M > 25M_{\odot}$ supernovae. The hypothesis also explains why Mn/Fe is not enhanced in the low-alpha stars (Nissen & Schuster 2011), which one might have expected if Type Ia SNe contribution of iron-peak elements is the

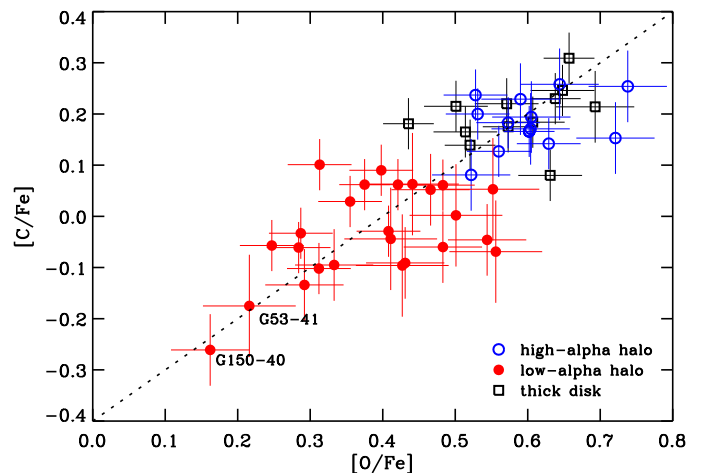


Fig. 11. $[C/Fe]$ versus $[O/Fe]$ for stars with $[Fe/H] < -0.8$. For stars with both $[O/H]_{6300}$ and $[O/H]_{7774}$ available, the average oxygen abundance has been applied.

explanation of the low-alpha stars. It is, however, difficult to see, how this hypothesis can explain why the difference in $[C/Fe]$, $[O/Fe]$, and $[\alpha/Fe]$ between high- and low-alpha stars increases as a function of increasing metallicity, which fact has a natural explanation with a delayed contribution of Fe from Type Ia SNe.

As seen from Figs. 9 and 10, thick-disk stars show the same trends of $[C/Fe]$ and $[O/Fe]$ as high-alpha halo stars. It is not possible to distinguish between these two populations from a chemical point of view. The thick-disk stars differ in kinematics from the high-alpha halo stars by having total space velocities, $V_{\text{total}} < 120 \text{ km s}^{-1}$ with respect to the LSR, whereas the high-alpha halo stars were selected to have $V_{\text{total}} > 180 \text{ km s}^{-1}$. It could be that both populations have been formed during a dissipative collapse of proto-Galactic gas clouds with each new generation of stars formed in increasingly flatter and more rotationally supported spheroids.

6.3. The $[C/O] - [O/H]$ diagram

The $[C/O] - [O/H]$ diagram shown in Fig. 12 is particularly useful when discussing the origin and Galactic evolution of carbon. Given that oxygen is exclusively produced in massive stars on a relatively short timescale, $\sim 10^7$ yr, the change in $[C/O]$ as a function of $[O/H]$ depends on the yields and timescales of carbon production in various types of stars (Chiappini et al. 2003; Akerman et al. 2004; Carigi et al. 2005; Cescutti et al. 2009; Carigi & Peimbert 2011).

As seen from Fig. 12, there is no systematic shift in $[C/O]$ between the high- and low-alpha halo populations; the stars distribute around a plateau of $[C/O] \approx -0.45$ when $[O/H] < -0.4$. This result came as a surprise. Assuming that the low $[C/Fe]$ and $[O/Fe]$ in low-alpha stars are due to Fe produced by Type Ia SNe, we had expected that low- and intermediate-mass AGB stars also had enough time to contribute carbon and raise $[C/O]$ in the low-alpha stars to higher values than in high-alpha stars. The explanation may be that intermediate-mass (4 - 8 M_{\odot}) AGB stars contribute very little to carbon (Kobayashi et al. 2011), and that the evolution timescale of low-mass (1 - 3 M_{\odot}) AGB stars, which do have a high carbon yield according to Kobayashi et al., is longer than the timescale for enriching the low-alpha stars with Fe from Type Ia SNe. Hence, it seems that carbon in high- and low-alpha halo stars as well as thick-disk stars with $[O/H] < -0.4$ was

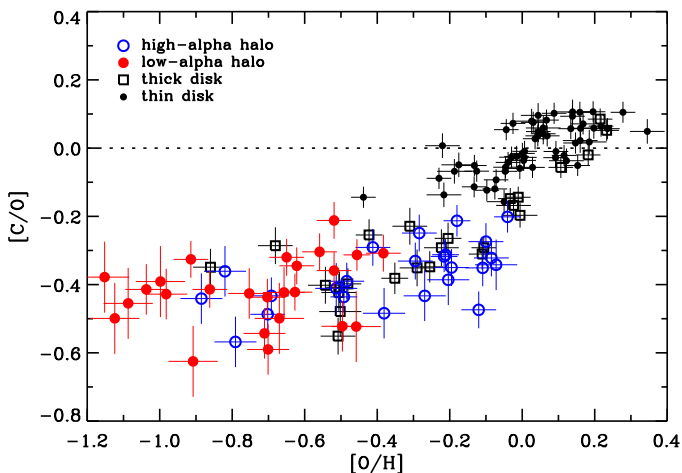


Fig. 12. $[C/O]$ versus $[O/H]$. For stars with both $[O/H]_{6300}$ and $[O/H]_{7774}$ available, the average oxygen abundance has been applied.

made mainly in high-mass stars ($M > 8 M_{\text{Sun}}$) with a C/O yield ratio corresponding to $[C/O] \approx -0.45$.

For the high-alpha halo and thick-disk stars, $[C/O]$ begins to rise at $[O/H] \sim -0.4$ and reaches $[C/O] \sim 0.0$ at $[O/H] \sim +0.2$. According to Cescutti et al. (2009), this increase can be explained as due to a metallicity dependent carbon yield of massive stars, but Akerman et al. (2004) and Carigi et al. (2005) ascribe the rise of $[C/O]$ to low-mass ($1 - 3 M_{\odot}$) AGB stars of low metallicity. The thin-disk stars lie on a different $[C/O]$ sequence shifted by ~ 0.2 dex to higher $[C/O]$ values. To explain this, carbon produced in both low-mass and massive stars has to be included. The model by Carigi et al. (2005) suggests that approximately half of the carbon in the more metal-rich thin-disk stars has come from low-mass stars and half from massive stars. A similar conclusion is reached by Cescutti et al. (2009). Still, it remains to be seen if chemical evolution models can reproduce the observed $[C/O]$ trends in detail.

The offset between thin- and thick-disk stars in the $[C/O] - [O/H]$ diagram has previously been found by Bensby & Feltzing (2006) in a study where the C and O abundances were derived from the forbidden $[C\text{I}] \lambda 8727$ and $[O\text{I}] \lambda 6300$ lines. Here it is confirmed with C and O abundances based on high-excitation permitted lines.

6.4. The C/O ratio in stars with planets

As mentioned in the introduction, there is much interest in the C/O ratio of stars hosting planets, because this ratio may have important effects on the structure and composition of the planets. High ratios ($C/O > 0.8$) were found in a significant fraction (10-15 %) of F and G dwarf stars by Delgado Mena et al. (2010) and Petigura & Marcy (2011) based on oxygen abundances derived from the forbidden $[O\text{I}] \lambda 6300$ line, but this was not confirmed by Nissen (2013), who derived oxygen abundances from the $O\text{I}$ triplet at 7774 \AA .

In this paper we have included a number of stars with no detection of planets. C/O as a function of $[\text{Fe}/\text{H}]$ for thin-disk stars is shown in Fig. 13 with oxygen abundances derived from either the $O\text{I}$ triplet at 7774 \AA (upper panel) or the $[O\text{I}] \lambda 6300$ line (lower panel). From linear regression, $y = A + Bx$, we

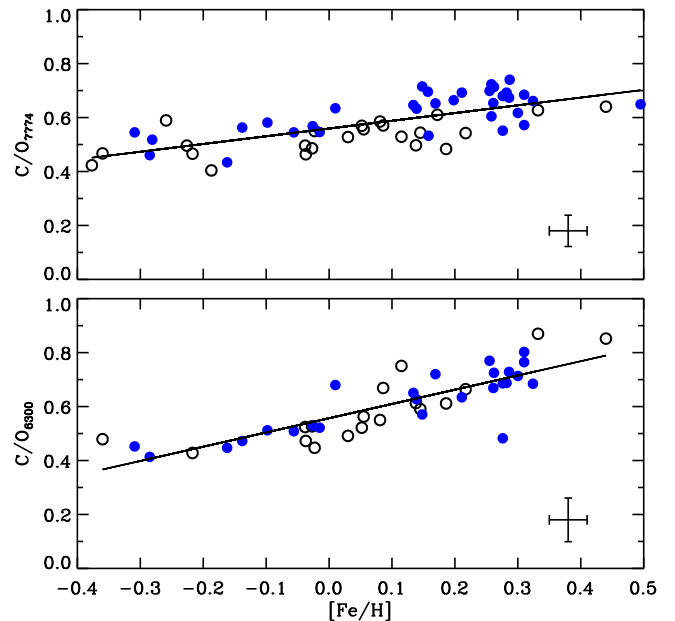


Fig. 13. The C/O ratio versus $[\text{Fe}/\text{H}]$ for thin-disk stars. Stars proven to have planets (see Table 4) are plotted with filled (blue) circles. In the upper panel, O abundances have been determined from the $O\text{I}$ triplet and in the lower panel from the $[O\text{I}] \lambda 6300$ line. The lines show the relations in Eqs. (2) and (3), respectively

obtain

$$C/O_{7774} = 0.559 (\pm 0.009) + 0.287 (\pm 0.039) [\text{Fe}/\text{H}] \quad (2)$$

with a standard deviation of ± 0.061 and

$$C/O_{6300} = 0.557 (\pm 0.012) + 0.529 (\pm 0.055) [\text{Fe}/\text{H}] \quad (3)$$

with a standard deviation of ± 0.068 .

In both cases, the zero-point (at $[\text{Fe}/\text{H}] = 0.0$) is close to the solar value, $(C/O)_{\odot} = 0.58$, determined from HARPS-FEROS spectra of reflected sunlight from Ceres and Ganymede. The slope of C/O_{6300} is, however, higher than that of C/O_{7774} , which is connected to the systematic differences between oxygen abundances derived from the $O\text{I}$ triplet and the forbidden line discussed in Sect. 5. In any case, both fits correspond to C/O values below 0.8 up to a metallicity of $[\text{Fe}/\text{H}] \approx +0.4$, and only two stars have C/O_{6300} above 0.8, which may be statistical deviations. Hence, we confirm the conclusion of Nissen (2013) that there is no evidence of the existence of stars with C/O values above 0.8, i.e., the critical limit for the formation of carbon planets (Bond et al. 2010).

The dispersions in C/O around the fitted lines in Fig. 13 correspond well to the errors of $[C/O]$ estimated in Table 6. Stars with planets detected⁶ tend, however, to lie above the fitted line in C/O_{7774} ; if only stars with planets are included in the regression, the zero-point of the fit becomes $A_{7774} = 0.586 \pm 0.013$ compared to $A_{7774} = 0.525 \pm 0.013$ for stars without planets. This difference is statistically significant at a 3-sigma level. On the other hand, a smaller difference is found in the case of C/O_{6300} . Here, the zero-points of the fits are $A_{6300} = 0.562 \pm 0.016$ for stars with planets and $A_{6300} = 0.552 \pm 0.017$ for stars without planets.

⁶ Based on the April 2014 version of the Exoplanet Orbit Database at <http://exoplanets.org> described by Wright et al. (2011)

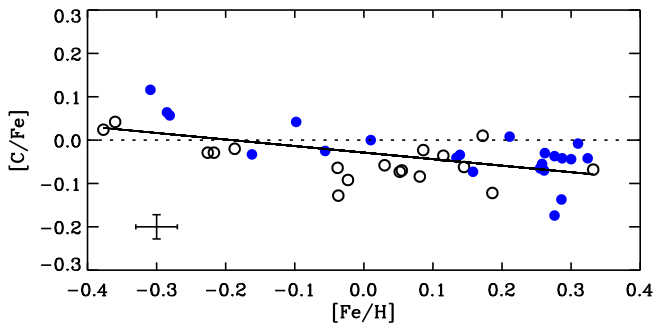


Fig. 14. $[C/Fe]$ versus $[Fe/H]$ for solar analog stars. Stars proven to have planets are plotted with filled (blue) circles. The line shows the relation in Eq. (4).

6.5. Scatter of $[C/Fe]$ and $[O/Fe]$ among solar analog stars

In a recent high-precision abundance work, Ramírez et al. (2014) found the slope of abundance ratios $[X/Fe]$ versus condensation temperature, T_C , of element X to vary with an amplitude of $\sim 10^{-4}$ dex K^{-1} . These variations were found for late F-type dwarfs, metal-rich solar analogs, and solar-twin stars. While the 50% condensation temperatures of C and O are 40 and 180 K, respectively, it is 1330 K for Fe in a solar-system composition gas (Lodders 2003). Hence, the results of Ramírez et al. imply that $[C/Fe]$ and $[O/Fe]$ should vary with an amplitude of approximately 0.1 dex, which magnitude may be detectable as a cosmic scatter in the $[C/Fe]$ and $[O/Fe]$ trends for our sample of F and G dwarf stars. Furthermore, the study of Meléndez et al. (2009) showed the Sun to have a high volatile-to-refractory ratio (corresponding to $[C/Fe] \sim [O/Fe] \sim 0.05$) relative to the ratio in 11 solar twins, which they suggest may be due to depletion of refractory elements when terrestrial planets formed.

In order to test these intriguing results, we have selected a sample of 40 solar “analog” stars, defined as thin-disk stars with effective temperatures within ± 200 K from the solar T_{eff} and metallicities in the range $-0.4 < [Fe/H] < +0.4$. The surface gravity of this sample ranges from $\log g = 3.90$ to 4.62, but the large majority ($N = 32$) of the stars have $\log g > 4.20$. The means of the atmospheric parameters are $\langle T_{\text{eff}} \rangle = 5760$ K and $\langle \log g \rangle = 4.35$, i. e. close to the solar parameters.

Figure 14 shows a plot of $[C/Fe]$ versus $[Fe/H]$ for these solar analogs. From linear regression we obtain

$$[C/Fe] = -0.029 (\pm 0.008) - 0.151 (\pm 0.035) [Fe/H] \quad (4)$$

with a standard deviation $\sigma[C/Fe] = 0.047$.

The upper panel of Fig. 15 shows the relation between $[O/Fe]_{7774}$ and $[Fe/H]$ for the sample of 40 solar analog stars and in the lower panel $[O/Fe]_{6300}$ versus $[Fe/H]$ is shown for the subsample of 32 solar analogs, which have O abundances determined from the $[O\text{I}] \lambda 6300$ line. The linear regressions are

$$[O/Fe]_{7774} = -0.003 (\pm 0.006) - 0.399 (\pm 0.029) [Fe/H] \quad (5)$$

with a standard deviation $\sigma[O/Fe]_{7774} = 0.039$, and

$$[O/Fe]_{6300} = -0.006 (\pm 0.009) - 0.533 (\pm 0.045) [Fe/H] \quad (6)$$

with $\sigma[O/Fe]_{6300} = 0.047$.

For $[O/Fe]_{7774}$ and $[O/Fe]_{6300}$, the standard deviations agree well with the errors estimated in Table 6, but in the case of $[C/Fe]$ the standard deviation of the regression (± 0.047 dex) is higher than the estimated error (± 0.028 dex). We note, in this connection, that an extension of the linear regression to include terms

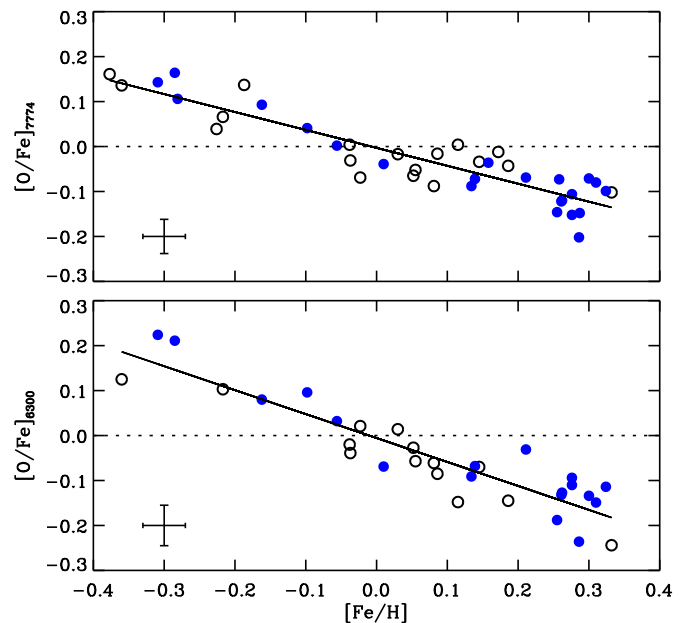


Fig. 15. $[O/Fe]$ versus $[Fe/H]$ for solar analog stars. Stars proven to have planets are plotted with filled (blue) circles. In the upper panel, O abundances have been determined from the $O\text{I}$ triplet and in the lower panel from the $[O\text{I}] \lambda 6300$ line. The lines correspond to Eqs. (5) and (6), respectively

in T_{eff} and $\log g$ does not decrease the standard deviation significantly (from ± 0.047 dex to ± 0.044 dex).

As seen from Figs. 14 and 15, stars with metallicities close to that of the Sun tend to fall below the fits suggesting that linear regression is not providing the right mean values of $[C/Fe]$ and $[O/Fe]$ for stars with $[Fe/H] \simeq 0.0$. For the group of 11 stars with $-0.1 < [Fe/H] < +0.1$ ⁷, the average values are $\langle [C/Fe] \rangle = -0.052$, $\langle [O/Fe]_{7774} \rangle = -0.029$, and $\langle [O/Fe]_{6300} \rangle = -0.016$. The small offsets of $[O/Fe]$ may be explained as due to accidental errors in the measured equivalent widths of the $O\text{I}$ triplet and $[O\text{I}] \lambda 6300$ lines in the solar spectrum, but to explain the offset in $[C/Fe]$ in this way, the solar EWs of the $C\text{I}$ lines at 5052 Å and 5380 Å would have to be overestimated by more than 2 mÅ. This is unlikely to be the case, because the HARPS spectrum of the Sun was obtained from reflected sunlight of Ceres and Ganymede in the same way as the stellar spectra. The spectra of these minor planets have S/N ratios of 350 and 250, respectively, and the EWs in the two spectra agree within 0.7 mÅ for the $\lambda 5052$ line and within 0.2 mÅ for the $\lambda 5380$ line. We also note that the stellar T_{eff} -scale at $[Fe/H] \simeq 0$ has to be wrong by ~ 150 K to explain the offset of $[C/Fe]$, which is much larger than the error of ± 15 K (estimated from solar twin stars) of the Cassagrande et al. (2010) IRFM calibration. Hence, it seems that the difference of $[C/Fe]$ between the Sun and stars with solar metallicity is real. Furthermore, we note that stars without detected planets in Fig. 14 tend to fall below stars proven to have planets. Fitting the two samples separately, we get

$$[C/Fe] = -0.003 (\pm 0.011) - 0.215 (\pm 0.047) [Fe/H] \quad (7)$$

for 22 stars with planets, and

$$[C/Fe] = -0.051 (\pm 0.011) - 0.132 (\pm 0.059) [Fe/H] \quad (8)$$

⁷ The average values of the atmospheric parameters of these stars, $\langle T_{\text{eff}} \rangle = 5808$ K, $\langle \log g \rangle = 4.43$, and $\langle [Fe/H] \rangle = 0.005$, are close to the solar values.

for 18 stars without planets. The difference in zero-points is significant at the 3-sigma level, and it is intriguing that stars with planets have the same $[C/Fe]$ at $[Fe/H] \approx 0.0$ as the Sun.

It is tempting to think that the scatter in $[C/Fe]$ and the possible systematic difference in $[C/Fe]$ between stars with and without planets are related to the variations in the volatile-to-refractory ratio found in the works of Meléndez et al. (2009) and Ramírez et al. (2014). However, similar “cosmic” variations are not seen for $[O/Fe]$; there is no significant difference in the trends of $[O/Fe]$ for stars with and without planets, and the scatter around the fitted lines is not larger than expected from the estimated error of $[O/Fe]$. This seems to rule out that the variations in $[C/Fe]$ (if real) can be explained as due to variations in the volatile-to-refractory ratio.

7. Conclusions

In this paper, we have determined precise C and O abundances for F and G main-sequence stars in the solar neighborhood belonging to four different populations defined from their sequences in the $[\alpha/Fe] - [Fe/H]$ diagram: thin- and thick-disk stars, high- and low-alpha halo stars. Based on the trends of $[C/Fe]$, $[O/Fe]$, and $[C/O]$, we make the following conclusions.

i) The high- and low-alpha halo populations are clearly separated in $[C/Fe]$ and $[O/Fe]$ for the metallicity range $-1.6 < [Fe/H] < -0.8$ (see Figs. 9 and 10). The high-alpha stars have approximately constant values of $[C/Fe] \approx 0.2$ and $[O/Fe] \approx 0.6$, whereas the low-alpha stars show decreasing trends in $[C/Fe]$ and $[O/Fe]$ as a function of increasing metallicity and present a higher dispersion in these abundance ratios than the high-alpha stars. These chemical properties and the kinematics of the stars can be explained in a scenario, where the high-alpha stars formed in situ in a dissipative collapse of proto-Galactic gas clouds, where mainly massive stars exploding as Type II SNe contributed to the chemical enrichment. The low-alpha stars, on the other hand, may have been accreted from dwarf galaxies with a relatively slow and bursting star formation history, so that Type Ia SNe started to contribute iron at $[Fe/H] \approx -1.6$.

ii) For metallicities below $[Fe/H] \approx -0.4$, stars with thick-disk kinematics follow the same trends in $[C/Fe]$ and $[O/Fe]$ as the high-alpha halo stars. In both populations, $[O/Fe]$ begins to decline at $[Fe/H] \approx -0.6$ because Type Ia SNe start to contribute iron at this metallicity. This suggest a similar origin of thick-disk and high-alpha halo stars, possibly during the dissipative collapse of proto-Galactic gas clouds.

iii) Although only a few metal-rich thick-disk stars are included in this study, we find clear evidence that thin- and thick disk stars (classified from $[\alpha/Fe]$) are separated in $[C/Fe]$ and $[O/Fe]$ in the metallicity range $-0.6 < [Fe/H] < +0.1$. This supports recent evidence of the existence of alpha-enhanced, metal-rich stars (Adibekyan et al. 2012; Bensby et al. 2014) that are older than the thin-disk stars (Haywood et al. 2013).

iv) The $[C/O] - [O/H]$ diagram (Fig. 12) shows no offset in $[C/O]$ between the high- and low-alpha halo stars, which suggests that mainly high-mass ($M > 8M_{\odot}$) stars have contributed C and O in these populations. The rise in $[C/O]$ at $[O/H] > -0.4$ for the high-alpha and thick-disk populations may be due to a metallicity dependent carbon yield of such high-mass stars (Cescutti et al. 2009) and/or the C contribution from low-mass stars (Carigi et al. 2005). The thin-disk stars show an offset in $[C/O]$ relative to the thick-disk stars due to additional C contribution from low-mass AGB star and massive stars of high metallicity (Carigi et al. 2005; Carigi & Peimbert 2011), which is made possible due to the younger age of the thin-disk population.

v) The C/O ratio of thin-disk stars (Fig. 13) shows a tight, increasing trend as a function of $[Fe/H]$, but even at the highest metallicities, $[Fe/H] \approx +0.4$, the ratio does not exceed 0.8, i.e., the critical value in a proto-planetary disk for the formation of carbon planets according to Bond et al. (2010). This confirms recent results obtained by Nissen (2013) and Teske et al. (2014). There is some evidence of higher C/O ratios in stars hosting planets than in stars without detected planets, but this needs to be confirmed.

vi) In a sample of solar analog stars, there is evidence of a small (0.05 ± 0.016 dex) systematic difference in $[C/Fe]$ between stars with and without detected planets. An attempt to explain this in terms of variations in the volatile-to-refractory element ratio (Meléndez et al. 2009; Ramírez et al. 2014) fails, because a similar difference in $[O/Fe]$ between stars with and without planets is not found.

Acknowledgements. This project is supported by the National Natural Science Foundation of China through Grant No. 11390371. P.E.N. acknowledges a visiting professorship at the National Astronomical Observatories in Beijing granted by the Chinese Academy of Sciences (Contract no. 6-1309001). L.C. thanks for the financial supports provided by CONACyT of Mexico (grant 129753) and by MINECO of Spain (AYA2010-16717 and AYA2011-22614). Funding for the Stellar Astrophysics Centre is provided by the Danish National Research Foundation (Grant agreement no.: DNR106). The research is supported by the ASTERoseismic Investigations with SONG and Kepler) funded by the European Research Council (Grant agreement no.: 267864). This research made use of the SIMBAD database operated at CDS, Strasbourg, France, the Exoplanet Orbit Database and the Exoplanet Data Explorer at <http://exoplanets.org>, and of data products from the Two Micron All Sky Survey, which is a joint project of the University of Massachusetts and the Infrared Processing and Analysis Center/California Institute of Technology, funded by NASA and the National Science Foundation.

References

- Adibekyan, V. Zh., Santos, N. C., Sousa, S. G., & Israelian, G. 2011, *A&A*, 535, L11
- Adibekyan, V. Zh., Sousa, S. G., Santos, N. C., et al. 2012, *A&A*, 545, A32
- Adibekyan, V. Zh., Figueira, P., Santos, N. C., et al. 2013, *A&A*, 554, A44
- Akerman, C. J., Carigi, L., Nissen, P. E., Pettini, M., & Asplund, M. 2004, *A&A*, 414, 931
- Allende Prieto, C., Lambert, D. L., & Asplund, M. 2001, *ApJ*, 556, L63
- Asplund, M. 2005, *ARA&A*, 43, 481
- Asplund, M., Grevesse, N., Sauval, A. J., & Scott, P. 2009, *ARA&A*, 47, 481
- Barklem, P. S. 2007, *A&A*, 462, 781
- Barklem, P. S. & Asplund-Johansson, J. 2005, *A&A*, 435, 373
- Barklem, P. S., Piskunov, N., & O’Mara, B. J. 2000, *A&AS*, 142, 467
- Bensby, T., & Feltzing, S. 2006, *MNRAS*, 367, 1181
- Bensby, T., Feltzing, S., & Lundström, I. 2004, *A&A*, 415, 155
- Bensby, T., Feltzing, S., Lundström, I., Ilyin, I. 2005, *A&A*, 433, 185
- Bensby, T., Feltzing, S., Oey, M. S. 2014, *A&A*, 562, A71
- Bond, H. E., Nelan, E. P., VandenBerg, D. A., Schaefer, G. H., & Harmer, D. 2013, *ApJ*, 765, L12
- Bond, J. C., O’Brien, D. P., & Laurotta, D. S. 2010, *ApJ*, 715, 1050
- Caffau, E., Ludwig, H.-G., Bonifacio, P., et al. 2010, *A&A*, 514, A92
- Caffau, E., Ludwig, H.-G., Malherbe, J.-M., et al. 2013, *A&A*, 554, A126
- Caffau, E., Ludwig, H.-G., Steffen, M., et al. 2008, *A&A*, 488, 1031
- Carigi, L., & Hernandez, X. 2008, *MNRAS*, 390, 582
- Carigi, L., Hernandez, X., & Gilmore, G. 2002, *MNRAS*, 334, 117
- Carigi, L., & Peimbert, M. 2011, *RMxAA*, 47, 139
- Carigi, L., Peimbert, M., Esteban, C., & García-Rojas, J. 2005, *ApJ*, 623, 213
- Carretta, E., Bragaglia, A., Gratton, R., & Lucatello, S. 2009, *A&A*, 505, 139
- Casagrande, L., Ramírez, I., Meléndez, J., Bessell, M., & Asplund, M. 2010, *A&A*, 512, A54
- Cayrel, R., Depagne, E., Spite, M., et al. 2004, *A&A*, 416, 1117
- Cescutti, G., Matteucci, F., McWilliam, A., & Chiappini, C. 2009, *A&A*, 505, 605
- Chiappini, C., Matteucci, F., & Meynet, G. 2003, *A&A*, 410, 257
- Delgado Mena, E., Israelian, G., González Hernández, J. I., et al. 2010, *ApJ*, 725, 2349
- Drawin, H.-W. 1968, *Zeitschrift für Physik*, 211, 404
- Fabbian, D., Asplund, M., Barklem, P. S., Carlsson, M., & Kiselman, D. 2009, *A&A*, 500, 1221

- Fortney, J. J. 2012, *ApJ*, 747, L27
- Fulbright, J. P., & Johnson, J. A. 2003, *ApJ*, 595, 1154
- García Pérez, A. E., Asplund, M., Primas, F., Nissen, P. E., & Gustafsson, B. 2006, *A&A*, 451, 621
- González Hernández, J. I., Israelian, G., Santos, N. C., et al. 2010 *ApJ*, 720, 1592
- González Hernández, J. I., Delgado-Mena, E., Sousa, S. G., et al. 2013 *A&A*, 552, A6
- Gustafsson, B., Edvardsson, B., Eriksson, K., et al. 2008, *A&A*, 486, 951
- Gustafsson, B., Karlsson, T., Olsson, E., Edvardsson, B., & Ryde, N. 1999, *A&A*, 342, 426
- Haywood, M., Di Matteo, P., Lehnert, M. D., Katz, D., & Gómez, A. 2013, *A&A* 560, A109
- Hibbert, A., Biémont, E., Godefroid, M., & Vaeck, N. 1991, *J. Phys. B*, 24, 3943
- Hibbert, A., Biémont, E., Godefroid, M., & Vaeck, N. 1993, *A&AS*, 99, 179
- Johansson, S., Litzén, U., Lundberg, H., & Zhang, Z. 2003, *ApJ*, 584, L107
- Kaufert, A., Stahl, O., Tubbesing, K., et al. 1999, *The Messenger*, 95, 8
- Kiselman, D. 1993, *A&A*, 275, 269
- Kobayashi, C., Ishigaki, M. N., Tominaga, N., & Nomoto, K. 2014 *ApJ*, 785, L5
- Kobayashi, C., Karakas, A. I., & Umeda, H. 2011, *MNRAS*, 414, 3231
- Kobayashi, C., Umeda, H., Nomoto, K., Tominaga, N., & Ohkubo, T. 2006, *ApJ*, 653, 1145
- Kuchner, M.J., & Seager, S. 2005, arXiv:astro-ph/0504214
- Lind, K., Bergemann, M., & Asplund, M. 2012, *MNRAS*, 427, 50
- Liu, S., Nissen, P. E., Schuster, W. J., et al. 2012, *A&A*, 541, A48
- Lodders, K. 2003, *ApJ*, 591, 1220
- Madhusudhan, N., Lee, K. K. M., & Mousis, O. 2012, *ApJ*, 759, L40
- Mashonkina, L., Gehren, T., Shi, J.-R., Korn, A. J., & Grupp, F. 2011, *A&A*, 528, A87
- Mayor, M., Pepe, F., Queloz, D., et al. 2003, *The Messenger*, 114, 20
- Meléndez, J. & Barbuy, B. 2009, *A&A*, 497, 611
- Meléndez, J., Asplund, M., Gustafsson, B., & Yong, D. 2009, *ApJ*, 704, L66
- Meynet, G., & Maeder, A. 2002, *A&A*, 390, 561
- Nissen, P. E. 2013, *A&A*, 552, A73
- Nissen, P. E., Primas, F., Asplund, M., & Lambert, D. L. 2002, *A&A*, 390, 235
- Nissen, P. E., & Schuster, W. J. 1997, *A&A*, 326, 751
- Nissen, P. E., & Schuster, W. J. 2010, *A&A*, 511, L10
- Nissen, P. E., & Schuster, W. J. 2011, *A&A*, 530, A15
- Nissen, P. E., & Schuster, W. J. 2012, *A&A*, 543, A28
- Nissen, P. E., & Schuster, W. J. 2014, in Proc. IAUS298 *Setting the scene for GAIA and LAMOST*, eds. S. Feltzing, G. Zhao, N. A. Walton, and P. A. Whitelock, (Cambridge Univ. Press) p. 65
- Olsen, E. H. 1983, *A&AS*, 54, 55
- Pereira, T. M. D., Asplund, M., & Kiselman, D. 2009, *A&A*, 508, 1403
- Perryman, M. A. C. (ed.) 1997, *The HIPPARCOS and TYCHO catalogues*, ESA SP-1200
- Petigura, E. A., & Marcy, G. W. 2011, *ApJ*, 735, 41
- Ramírez, I., Allende Prieto, C., & Lambert, D. L. 2013, *ApJ*, 764, 78
- Ramírez, I., & Meléndez, J. 2005, *ApJ*, 626, 465
- Ramírez, I., Meléndez, J., & Chanamé, J. 2012, *ApJ*, 757, 164
- Ramírez, I., Meléndez, J., & Asplund, M. 2014, *A&A*, 561, A7
- Reddy, B. E., Lambert, D. L., & Allende Prieto, C. 2006, *MNRAS*, 367, 1329
- Schuler, S. C., King, J. R., Hobbs, L. M., Pinsonneault, M. H. 2004, *ApJ*, 602, L117
- Schuler, S. C., King, J. R., Terndrup, D. M., et al. 2006, *ApJ*, 636, 432
- Schuster, W. J., Moreno, E., Nissen, P. E., & Pichardo, B. 2012 *A&A*, 538, A21
- Scott, P., Asplund, M., Grevesse, N., & Sauval, J. 2009, *ApJ*, 691, L119
- Shi, J. R., Zhao, G., & Chen, Y. Q. 2002, *A&A*, 381, 982
- Skrutskie, M. F., Cutri, R. M., Stiening, R., et al. 2006, *AJ*, 131, 1163
- Sousa, S. G., Santos, N. C., Mayor, M., et al. 2008, *A&A*, 487, 373
- Sousa, S. G., Santos, N. C., Israelian, G., et al. 2011a, *A&A*, 526, A99
- Sousa, S. G., Santos, N. C., Israelian, G., Mayor, M., & Udry, S. 2011b, *A&A*, 533, A141
- Takeda, Y., & Honda, S. 2005, *PASJ*, 57, 65
- Takeda, Y. & Takada-Hidai, M. 2013, *PASJ*, 65, 65
- Teske, J. K., Cunha, K., Schuler, S. C., Griffith, C. A., & Smith, V. V. 2013, *ApJ*, 778, 132
- Teske, J. K., Cunha, K., Smith, V. V., Schuler, S. C., & Griffith, C. A. 2014, *ApJ*, 788, 39
- Tolstoy, E., Hill, V., & Tosi, M. 2009, *ARA&A*, 47, 371
- Unsöld, A. 1955, *Physik der Sternatmosphären*, 2nd ed. (Berlin: Springer Verlag)
- van den Hoek, L. B., & Groenewegen, M. A. T. 1997, *A&AS*, 123, 305
- van Leeuwen, F. 2007, *Hipparcos, the New Reduction of the Raw Data*, (Astrophys. Space Sci. Library, vol. 350; Dordrecht, Springer)
- Wright, J. T., Fakhouri, O., Marcy, G. W., et al. 2011, *PASP*, 123, 412
- Yi, S. K., Kim, Y. -C., & Demarque, P. 2003, *ApJS*, 144, 259

Table 2. ESO observing program numbers, S/N ratios of spectra, and measured equivalent widths for the HARPS-FEROS sample.

ID	HARPS		FEROS	 EW(mÅ)					[O I]+Ni ^a	[O I] ^b
	Program	S/N	Program	S/N	C I ₅₀₅₂	C I ₅₃₈₀	O I ₇₇₇₂	O I ₇₇₇₄	O I ₇₇₇₅		
HD 1237	72.C-0488	350	60.A-9700	200	30.9	16.8	59.1	50.2	36.4	6.0	3.5
HD 4208	-	200	83.A-9011	200	21.4	11.9	52.3	42.6	33.6		
HD 4307	-	500	-	250	32.0	18.9	78.1	66.1	55.2	5.9	4.9
HD 4308	-	600	74.D-0086	500	25.5	14.1	68.1	58.5	42.4		
HD 14374	-	350	83.A-9011	200	22.4	11.6	43.6	38.1	31.5	5.0	3.2
HD 16141	-	300	83.A-9011	250	45.2	27.9	86.3	75.7	58.6		
HD 20782	-	900	-	200	33.5	19.9	72.2	59.5	49.3	5.4	4.0
HD 23079	-	900	84.A-9004	200	34.1	19.7	80.8	68.5	51.8	4.2	3.2
HD 28185	-	500	83.A-9011	250	44.5	26.9	71.7	62.7	46.2	8.6	5.1
HD 30177	-	250	84.A-9004	200	48.5	31.0	72.2	62.0	53.3		
HD 30306	-	500	82.C-0446	150	38.5	21.5	63.8	54.5	45.8	7.5	4.1
HD 40397	-	300	78.D-0760	200	29.4	16.7	61.0	51.3	36.4	6.4	4.6
HD 52265	-	250	80.A-9021	350	59.1	38.9	109.2	95.6	83.1		
HD 65216	-	500	83.A-9003	250	22.2	12.4	54.4	50.3	35.7	4.4	3.2
HD 65907	88.C-0011	900	78.D-0760	150	35.2	19.6	89.2	75.2	60.5	5.2	4.5
HD 69830	72.C-0488	800	77.C-0573	300	23.1	12.7	42.0	37.2	28.1	5.5	3.5
HD 73256	-	1100	83.A-9003	200	39.7	22.5	61.5	54.5	41.3	8.1	4.0
HD 75289	-	650	84.A-9003	500	57.3	36.4	108.2	95.4	78.3	5.5	3.2
HD 77110	82.C-0212	500	76.B-0416	150	18.1	9.4	60.2	52.3	39.0	5.0	4.4
HD 78538	72.C-0488	350	77.D-0525	150	27.7	15.5	67.2	60.9	41.6	4.4	3.0
HD 82943	-	700	84.A-9004	300	55.0	35.4	100.2	87.2	72.8	6.9	4.1
HD 89454	-	900	77.D-0525	150	35.9	20.5	68.1	65.0	49.3	5.9	3.2
HD 92788	-	400	80.A-9021	250	49.0	30.0	81.1	70.1	58.3	8.5	4.6
HD 94151	-	400	77.D-0525	200	33.0	19.3	59.4	58.0	37.8	5.7	3.3
HD 96423	-	550	-	150	38.7	22.7	74.4	60.5	50.3	6.8	4.1
HD 102365	60.A-9036	450	88.C-0892	250	23.0	13.5	54.3	45.6	33.8	4.6	3.6
HD 108147	72.C-0488	650	83.A-9013	250	55.6	35.0	114.9	98.1	80.9	4.2	2.7
HD 110668	-	120	77.D-0525	150	49.0	29.7	85.5	78.6	60.6		
HD 111232	-	550	-	250	19.6	10.5	54.8	45.5	33.0		
HD 114613	-	700	80.D-2002	250	50.3	30.7	83.5	76.6	63.1	9.7	6.7
HD 114729	-	900	-	350	31.6	18.2	76.0	64.9	52.6	6.2	5.3
HD 114853	-	750	77.D-0525	150	22.4	12.8	58.0	47.2	36.2		
HD 115617	72.D-0707	450	86.D-0460	150	27.3	15.7	52.7	48.7	31.4	6.1	4.1
HD 117207	72.C-0488	200	83.A-9013	200	43.8	26.5	74.3	61.1	51.5		
HD 117618	-	600	-	300	44.8	28.1	92.1	79.4	60.2	5.0	3.4
HD 125184	-	850	85.C-0557	250	50.5	32.9	79.6	73.0	58.7	9.4	5.0
HD 125612	-	350	77.D-0525	200	45.1	27.7	88.8	76.0	62.0	7.2	4.4
HD 126525	-	500	-	150	29.8	16.8	59.2	52.9	35.4	5.7	4.1
HD 128674	-	500	76.B-0416	150	17.2	8.8	45.5	39.4	24.3	3.6	2.7
HD 134664	-	600	77.D-0525	150	37.6	21.8	75.3	70.5	48.8	5.5	3.7
HD 134987	-	550	83.A-9013	250	53.7	33.8	87.5	76.4	57.8	8.9	4.8
HD 136352	-	700	89.C-0440	350	26.2	15.1	65.5	56.9	43.2	5.8	5.0
HD 140901	-	650	78.A-9059	200	33.2	19.2	60.1	53.5	42.8	5.7	3.1
HD 145666	-	550	77.D-0525	150	34.3	20.4	80.6	67.6	57.3	4.4	3.1
HD 146233	-	1000	78.A-9007	300	35.8	21.2	73.1	62.2	51.3	5.5	3.6
HD 157347	-	450	89.C-0440	500	32.0	19.1	66.1	56.9	44.3	6.2	4.2
HD 160691	73.D-0578	600	83.A-9013	250	54.1	35.1	89.2	77.1	65.6	9.5	5.5
HD 168443	72.C-0488	600	83.A-9003	300	41.6	25.5	72.9	65.5	50.7	9.8	7.1
HD 169830	-	550	83.A-9013	350	70.5	46.9	139.3	123.8	102.5	6.2	4.8
HD 179949	-	450	85.C-0743	450	59.7	38.2	118.5	101.9	83.4		
HD 183263	75.C-0332	500	79.A-9013	250	57.4	37.5	98.7	84.4	67.7		
HD 190248	74.D-0380	700	77.A-9009	150	52.7	31.3	74.8	68.0	56.3	10.1	4.6
HD 196050	72.C-0488	950	83.A-9011	300	56.8	37.1	97.5	82.6	69.5	8.2	5.0
HD 196761	-	750	77.A-9009	200	17.5	8.9	36.2	30.0	21.9		
HD 202206	-	700	83.A-9011	200	43.3	26.7	74.7	67.0	48.7	6.8	3.3
HD 203608	77.D-0720	600	85.A-9027	300	19.7	11.0	70.5	61.2	48.5	2.0	1.8
HD 206172	72.C-0488	200	77.C-0192	120	20.4	11.3	53.8	50.4	34.0		

Table 2. continued

ID	HARPS		FEROS	 <i>EW</i> (mÅ)					[O I]+Ni ^a	[O I] ^b
	Program	<i>S/N</i>	Program	<i>S/N</i>	C I ₅₀₅₂	C I ₅₃₈₀	O I ₇₇₇₂	O I ₇₇₇₄	O I ₇₇₇₅		
HD 207129	-	800	60.A-9122	300	35.7	20.7	80.7	67.4	54.0	5.0	3.6
HD 210277	-	900	-	200	41.1	25.0	65.1	57.7	44.4	8.5	4.8
HD 212301	82.C-0312	350	85.C-0743	350	58.4	37.2	112.8	97.6	81.8		
HD 213240	72.C-0488	300	83.A-9011	200	51.9	33.5	99.1	82.5	71.1	6.9	4.7
HD 216435	-	700	-	200	61.2	40.1	108.9	96.5	77.1	7.7	4.8
HD 216777	-	330	77.C-0192	120	17.2	8.9	46.5	39.3	32.9		
HD 216437	80.D-0408	700	-	200	36.7	21.6	52.4	47.3	37.3	8.9	5.5
HD 216770	72.C-0488	600	-	120	54.9	36.9	96.3	81.8	65.7	8.5	3.5
HD 222669	-	650	77.D-0525	150	39.5	23.6	79.0	71.9	55.2	5.2	3.4

Notes. ^(a) The EW of the [O I] + Ni I blend at 6300.3 Å.

^(b) The EW of [O I] λ6300.3 after correcting for the contribution of the Ni I line.

Table 3. Equivalent widths for the UVES-FIES sample of halo and thick-disk stars.

ID $EW(m\text{\AA})$ $EW(m\text{\AA})$ $EW(m\text{\AA})$			
	C I ₅₀₅₂	C I ₅₃₈₀	ref. ^a	O I ₇₇₇₂	O I ₇₇₇₄	O I ₇₇₇₅	ref. ^b	[O I]+Ni ^c	[O I] ^d	ref. ^e
BD-21 3420	7.4	4.1	U	49.4	43.4	34.6	R,E	2.2	2.1	U
CD-33 3337	7.2	3.7	U	51.5	42.6	31.6	R,E			
CD-43 6810	33.7	18.6	U	94.7	81.6	65.0	R	5.1	4.6	U
CD-45 3283	3.2	2.0	U	32.2	26.1	20.1	R,E			
CD-51 4628	3.3	2.4	U	41.5	33.2	23.8	R			
CD-57 1633	7.9	3.8	U,H	47.1	40.2	29.7	R,E			
CD-61 0282	3.0	1.5	U	35.8	28.9	22.1	R,E			
G05-19	3.7	2.1	U	40.1	33.1	23.1	R			
G05-36	6.8		F	52.0	45.0	39.0	R			
G05-40	15.0	8.0	U	66.1	57.5	44.0	R,E			
G15-23	3.0		F	21.9	18.8	13.5	R			
G18-28	7.3		U	34.9		22.2	R			
G18-39	4.8	2.1	U	41.8	36.9	25.7	U			
G20-15	3.0	1.5	U	30.4	27.7	16.9	R			
G21-22	6.2	1.9	F							
G24-13	11.8	6.6	F	62.8	56.5	42.0	R			
G31-55	5.2	3.2	F	40.4	32.8	22.3	R			
G46-31	12.3	6.3	U	58.0	50.3	36.9	E	2.5	2.3	U
G49-19	23.0	11.5	F							
G53-41	2.6	1.6	F		21.8	14.1	R			
G56-30	6.4	3.3	F							
G56-36	10.4	4.8	F	58.6	50.0	38.5	R			
G57-07	20.8	11.6	F							
G63-26	4.5	1.9	U							
G66-22	2.3	1.3	U	20.0	18.6	10.1	R			
G74-32	15.3	7.7	F							
G75-31	7.2		F	55.7	44.4	34.3	U			
G81-02	18.3	9.2	F							
G82-05	5.4	2.3	U	24.0	20.0	13.0	R			
G85-13	13.7	7.8	F	59.0	49.1	39.5	R			
G87-13	6.4	1.9	F							
G96-20	20.9	11.5	F							
G98-53	9.9	5.3	F							
G99-21	12.7	6.9	F	50.7	39.1	31.8	R			
G112-43	6.7	3.3	U	47.2	40.0	28.0	R			
G112-44	3.5	2.4	U							
G114-42	3.2	2.0	U							
G119-64	3.5		F	37.9	34.3	22.8	R			
G121-12	6.4	3.2	U							
G127-26	24.1	13.3	F							
G150-40	6.8	4.7	F	52.8	48.0	38.0	R			
G159-50	8.6	4.3	U	41.9		24.7	R			
G161-73	7.0		F							
G170-56	10.4	5.1	F	58.9	50.1	36.9	R			
G176-53				21.9		10.4	R			
G180-24	5.5	3.3	F	44.1	38.0	29.0	R			
G187-18	13.8	7.8	F							
G188-22	6.0	2.8	U	53.0	43.3	33.1	R			
HD3567	6.1	3.0	U	49.9	41.8	31.1	R,U			
HD17820	19.3	10.1	U	71.3	61.9	45.4	R,E	4.0	3.6	U
HD22879	13.0	7.0	U,H	62.1	53.2	41.4	R,F			
HD25704	13.6	7.4	U,H	62.3	49.4	37.4	R,E	2.6	2.4	U,H
HD51754	20.8	11.2	U,H	70.4	62.7	44.3	R	3.9	3.4	U,H
HD59392	3.4	1.2	U	37.0	28.5	19.1	R			
HD76932	13.4	7.3	U	66.0	56.9	44.1	R,U	3.5	3.3	U
HD97320	9.6	4.9	U,H	55.6	45.7	35.9	R,F			
HD103723	11.0	5.9	U	57.8	49.7	37.9	U			

Table 3. continued

ID $EW(m\text{\AA})$		ref. ^a $EW(m\text{\AA})$			ref. ^b $EW(m\text{\AA})$		ref. ^e
	C I ₅₀₅₂	C I ₅₃₈₀		O I ₇₇₇₂	O I ₇₇₇₄	O I ₇₇₇₅		[O I]+Ni ^c	[O I] ^d	
HD105004	10.3	5.5	U	45.9	37.2	28.8	U			
HD106516	24.7	12.9	U	98.0	84.2	66.7	R,E			
HD111980	8.9	5.1	U	62.0	51.6	38.4	R	2.9	2.7	U
HD113679	17.5	9.5	U,H	69.3	60.0	44.8	R,E	4.9	4.4	U,H
HD114762A	18.7	10.1	U	70.4	60.7	46.6	R			
HD120559	6.6	3.5	U	31.5	29.2	20.7	R,E	3.7	3.4	U
HD121004	13.1	7.2	U,H	57.7	47.5	35.0	R,E	3.8	3.4	U,H
HD126681	3.1	2.1	U,H	29.4	24.4	16.7	R,E			
HD132475	3.8	1.7	U	38.9	29.7	21.2	R			
HD148816	19.1	10.3	U,H	73.3	62.0	46.3	R			
HD159482	14.4	7.9	F	64.7	54.9	43.6	R			
HD160693	20.7	11.1	F	72.0	60.2	45.7	R			
HD163810	2.1		U	20.0		12.2	R			
HD175179	17.6	9.6	U	70.3	64.3	42.3	R	4.3	3.9	U
HD179626	9.5	5.4	U	59.0	50.2	39.6	R			
HD189558	6.6	3.2	U	51.7	41.5	30.1	R			
HD193901	3.8	2.2	U,H	32.4	26.5	18.9	R			
HD194598	5.7	2.6	U	45.6	38.2	27.6	R			
HD199289	8.4	4.3	U,H	52.0	44.3	33.1	R	2.4	2.2	U,H
HD205650	5.7	3.1	U	42.2	32.4	24.4	R			
HD219617	2.1		U	30.3	26.9	17.9	R			
HD222766	9.9	6.6	U	42.9	37.2	25.0	R			
HD230409	4.7		F	27.0	23.0	18.0	R			
HD233511				33.2	30.1	18.3	R			
HD237822	20.9	12.8	F							
HD241253	7.5	3.8	U	52.4	41.3	33.3	R,E			
HD250792A				29.7	22.9		R			
HD284248	2.8	1.7	U	30.9	26.3	18.1	R			

Notes. ^(a) Reference for EWs of C I lines: U, UVES; F, FIES; H, HARPS.

^(b) Reference for EWs of O I lines: R, Ramirez et al. (2012); E, EMMI; U, UVES; F, FEROS.

^(c) The EW of the [O I] + Ni I blend at 6300.3 Å.

^(d) The EW of [O I] λ 6300.3 after correcting for the contribution of the Ni I line.

^(e) Reference for EWs of the [O I] line: U, UVES; H, HARPS.

Table 4. Atmospheric parameters and abundances for the HARPS-FEROS sample of disk stars.

ID	T_{eff} (K)	$\log g$	[Fe/H]	ξ_{turb} km s^{-1}	[C/H] LTE	[C/H] non-LTE	[O/H] $_{7774}$ LTE	[O/H] $_{7774}$ non-LTE	[O/H] $_{6300}$	Pop. ^a	N_{planet} ^b
HD1237	5507	4.56	0.14	1.25	0.09	0.09	0.09	0.16	0.07	D	0
HD4208	5688	4.53	-0.28	1.02	-0.22	-0.22	-0.23	-0.17		D	1
HD4307	5828	4.02	-0.22	1.23	-0.24	-0.25	-0.09	-0.15	-0.11	D	0
HD4308	5705	4.36	-0.35	1.00	-0.19	-0.19	-0.04	-0.02		C	1
HD14374	5466	4.58	-0.03	0.84	-0.07	-0.07	-0.08	0.01	-0.02	D	0
HD16141	5722	4.10	0.16	1.13	0.09	0.09	0.18	0.12		D	1
HD20782	5784	4.35	-0.06	1.02	-0.08	-0.08	-0.04	-0.05	-0.02	D	1
HD23079	5988	4.38	-0.14	1.15	-0.18	-0.18	-0.13	-0.17	-0.09	D	1
HD28185	5640	4.35	0.21	0.94	0.22	0.22	0.14	0.14	0.18	D	1
HD30177	5550	4.39	0.50	0.92	0.39	0.39	0.33	0.34		D	1
HD30306	5544	4.38	0.22	0.90	0.16	0.16	0.16	0.19	0.10	D	0
HD40397	5474	4.38	-0.12	0.96	0.05	0.05	0.11	0.16	0.05	C	0
HD52265	6129	4.32	0.26	1.27	0.15	0.14	0.18	0.04		D	2
HD65216	5658	4.52	-0.16	0.98	-0.20	-0.19	-0.12	-0.07	-0.08	D	2
HD65907	5998	4.41	-0.33	1.08	-0.15	-0.16	0.00	-0.05	0.03	C	0
HD69830	5460	4.55	-0.03	0.63	-0.04	-0.04	-0.12	-0.03	0.00	D	3
HD73256	5453	4.46	0.31	1.13	0.29	0.29	0.24	0.30	0.17	D	1
HD75289	6121	4.34	0.28	1.32	0.11	0.11	0.16	0.03	0.03	D	1
HD77110	5738	4.39	-0.51	0.87	-0.40	-0.40	-0.17	-0.14	-0.07	C	0
HD78538	5790	4.50	-0.04	1.06	-0.17	-0.17	-0.08	-0.07	-0.08	D	0
HD82943	5958	4.38	0.26	1.21	0.19	0.19	0.22	0.14	0.13	D	3
HD89454	5699	4.53	0.19	0.94	0.06	0.06	0.12	0.14	0.04	D	0
HD92788	5691	4.35	0.30	1.05	0.26	0.26	0.25	0.23	0.17	D	2
HD94151	5621	4.50	0.09	0.89	0.06	0.06	0.03	0.07	0.00	D	0
HD96423	5689	4.39	0.14	0.96	0.08	0.08	0.11	0.11	0.08	D	0
HD102365	5690	4.46	-0.31	0.91	-0.19	-0.19	-0.21	-0.17	-0.09	D	1
HD108147	6218	4.39	0.17	1.35	0.05	0.05	0.14	0.00	-0.05	D	1
HD110668	5808	4.39	0.17	1.08	0.18	0.18	0.20	0.16		D	0
HD111232	5543	4.43	-0.48	0.90	-0.20	-0.20	-0.07	-0.01		C	1
HD114613	5700	3.90	0.14	1.33	0.11	0.10	0.16	0.07	0.07	D	1
HD114729	5790	4.07	-0.28	1.27	-0.21	-0.22	-0.07	-0.12	-0.07	D	1
HD114853	5744	4.46	-0.23	0.97	-0.25	-0.25	-0.22	-0.19		D	0
HD115617	5534	4.41	-0.01	0.91	-0.03	-0.03	-0.07	-0.01	0.01	D	3
HD117207	5632	4.34	0.26	0.97	0.20	0.20	0.18	0.19		D	1
HD117618	5962	4.32	0.01	1.18	0.01	0.01	0.04	-0.03	-0.06	D	2
HD125184	5610	4.07	0.33	1.14	0.27	0.26	0.27	0.23	0.09	D	0
HD125612	5872	4.45	0.28	1.13	0.10	0.10	0.17	0.12	0.18	D	3
HD126525	5650	4.41	-0.10	0.92	-0.06	-0.06	-0.09	-0.06	0.00	D	1
HD128674	5600	4.48	-0.36	0.82	-0.32	-0.32	-0.30	-0.22	-0.23	D	0
HD134664	5805	4.39	0.05	1.11	-0.01	-0.01	0.02	0.00	0.00	D	0
HD134987	5710	4.28	0.31	1.08	0.30	0.30	0.27	0.23	0.16	D	2
HD136352	5728	4.36	-0.39	1.05	-0.18	-0.18	-0.08	-0.07	0.00	C	3
HD140901	5582	4.47	0.12	0.95	0.08	0.08	0.08	0.12	-0.03	D	0
HD145666	5918	4.47	-0.04	1.09	-0.10	-0.10	-0.01	-0.03	-0.06	D	0
HD146233	5820	4.47	0.05	1.01	-0.02	-0.02	-0.01	-0.01	0.03	D	0
HD157347	5688	4.41	0.03	0.96	-0.03	-0.03	0.00	0.01	0.04	D	0
HD160691	5737	4.23	0.32	1.11	0.28	0.28	0.28	0.22	0.21	D	4
HD168443	5522	4.06	0.07	1.02	0.17	0.16	0.23	0.22	0.14	C	2
HD169830	6319	4.08	0.15	1.58	0.11	0.10	0.28	0.01	0.11	D	2
HD179949	6182	4.36	0.20	1.34	0.12	0.12	0.21	0.06		D	1
HD183263	5889	4.29	0.29	1.23	0.25	0.25	0.22	0.14		D	2
HD190248	5572	4.31	0.44	0.94	0.38	0.38	0.34	0.34	0.22	D	0
HD196050	5862	4.22	0.26	1.16	0.24	0.23	0.23	0.14	0.14	D	1
HD196761	5486	4.56	-0.26	0.75	-0.22	-0.21	-0.32	-0.22		D	0
HD202206	5746	4.44	0.29	1.11	0.15	0.15	0.09	0.08	0.05	D	2
HD203608	6180	4.35	-0.66	1.30	-0.57	-0.58	-0.41	-0.45	-0.42	D	0
HD206172	5662	4.62	-0.19	0.84	-0.21	-0.21	-0.11	-0.05		D	0

Table 4. continued

ID	T_{eff} (K)	$\log g$	[Fe/H]	ξ_{turb} km s^{-1}	[C/H] LTE	[C/H] non-LTE	[O/H] $_{7774}$ LTE	[O/H] $_{7774}$ non-LTE	[O/H] $_{6300}$	Pop. ^a	N_{planet} ^b
HD207129	5941	4.42	-0.02	1.06	-0.11	-0.12	-0.06	-0.09	0.00	D	0
HD210277	5479	4.34	0.24	0.84	0.28	0.28	0.26	0.29	0.17	C	1
HD212301	6162	4.35	0.16	1.35	0.11	0.10	0.17	0.03		D	1
HD213240	5918	4.15	0.13	1.25	0.10	0.09	0.16	0.05	0.04	D	1
HD216435	5942	4.08	0.25	1.36	0.20	0.19	0.26	0.11	0.07	D	1
HD216437	5802	4.17	0.28	1.14	0.24	0.24	0.25	0.17	0.17	D	1
HD216770	5424	4.53	0.37	0.79	0.29	0.30	0.18	0.26	0.17	C	1
HD216777	5656	4.47	-0.38	0.89	-0.35	-0.35	-0.28	-0.22		D	0
HD222669	5908	4.48	0.08	1.01	0.00	0.00	0.02	-0.01	0.02	D	0

Notes. ^(a) Population classification: C, thick-disk; D, thin-disk.

^(b) Number of planets detected, (<http://exoplanets.org>, April 2014).

Table 5. Atmospheric parameters and abundances for the UVES-FIES sample of halo and thick-disk stars.

ID	T_{eff} (K)	$\log g$	[Fe/H]	ξ_{turb} km s ⁻¹	[C/H] LTE	[C/H] non-LTE	[O/H] ₇₇₇₄ LTE	[O/H] ₇₇₇₄ non-LTE	[O/H] ₆₃₀₀	Pop. ^a	Bin. ^b
BD-21 3420	5909	4.30	-1.14	1.12	-0.91	-0.91	-0.50	-0.49	-0.52	C	
CD-33 3337	6112	3.86	-1.37	1.56	-1.19	-1.21	-0.81	-0.86		C	
CD-43 6810	6059	4.32	-0.44	1.24	-0.24	-0.24	0.00	-0.08	0.00	A	
CD-45 3283	5685	4.61	-0.93	0.95	-1.02	-1.02	-0.60	-0.50		B	
CD-51 4628	6296	4.29	-1.32	1.31	-1.40	-1.41	-0.98	-0.98		B	
CD-57 1633	5981	4.29	-0.91	1.08	-0.96	-0.97	-0.64	-0.62		B	
CD-61 0282	5869	4.34	-1.25	1.19	-1.29	-1.29	-0.75	-0.70		B	
G05-19	5770	4.28	-1.19	1.17	-1.25	-1.25	-0.78	-0.71		B	
G05-36	6139	4.22	-1.25	1.29	-1.12	-1.12	-0.67	-0.69		A	
G05-40	5892	4.20	-0.83	1.12	-0.62	-0.63	-0.27	-0.29		A	
G15-23	5373	4.63	-1.12	0.90	-0.87	-0.87	-0.52	-0.38		A	
G18-28	5443	4.49	-0.85	0.88	-0.59	-0.59	-0.31	-0.20		A	SB1
G18-39	6175	4.21	-1.41	1.37	-1.32	-1.33	-0.88	-0.88		A	
G20-15	6162	4.32	-1.50	1.50	-1.44	-1.45	-1.07	-1.04		B	
G21-22	6021	4.27	-1.10	1.30	-1.19	-1.19				B	
G24-13	5764	4.38	-0.73	0.86	-0.59	-0.59	-0.14	-0.12		A	
G31-55	5731	4.35	-1.12	1.26	-0.92	-0.92	-0.58	-0.51		A	
G46-31	6017	4.29	-0.83	1.30	-0.76	-0.77	-0.50	-0.51	-0.41	B	SB1
G49-19	5863	4.32	-0.55	1.12	-0.37	-0.37				A	SB1
G53-41	5975	4.29	-1.21	1.20	-1.38	-1.39	-1.06	-1.00		B	
G56-30	5935	4.29	-0.90	1.22	-1.02	-1.02				B	
G56-36	6067	4.33	-0.94	1.33	-0.87	-0.88	-0.51	-0.52		B	
G57-07	5755	4.33	-0.48	0.99	-0.33	-0.33				A	
G63-26	6175	4.17	-1.58	1.65	-1.36	-1.37				A	
G66-22	5297	4.46	-0.88	0.78	-0.98	-0.98	-0.59	-0.46		B	
G74-32	5864	4.41	-0.74	1.04	-0.54	-0.54				A	
G75-31	6135	4.02	-1.04	1.28	-1.17	-1.18	-0.72	-0.75		B	
G81-02	5967	4.24	-0.69	1.21	-0.57	-0.57				A	
G82-05	5338	4.51	-0.78	0.80	-0.69	-0.69	-0.51	-0.38		B	
G85-13	5709	4.46	-0.60	0.87	-0.46	-0.46	-0.15	-0.11		A	
G87-13	6217	4.11	-1.10	1.42	-1.34	-1.35				B	
G96-20	6445	4.46	-0.90	1.42	-0.62	-0.63				A	
G98-53	5954	4.26	-0.89	1.20	-0.83	-0.84				B	
G99-21	5559	4.46	-0.68	0.79	-0.41	-0.41	-0.16	-0.09		A	
G112-43	6209	4.02	-1.27	1.17	-1.23	-1.24	-0.88	-0.91		B	
G112-44	5936	4.28	-1.31	1.10	-1.21	-1.21				B	
G114-42	5721	4.40	-1.12	1.19	-1.10	-1.11				B	
G119-64	6333	4.14	-1.50	1.40	-1.53	-1.54	-1.08	-1.09		B	
G121-12	6041	4.25	-0.94	1.26	-1.09	-1.10				B	
G127-26	5886	4.20	-0.53	1.11	-0.37	-0.38				A	
G150-40	6080	4.11	-0.82	1.31	-1.07	-1.08	-0.63	-0.66		B	
G159-50	5713	4.44	-0.94	1.03	-0.70	-0.70	-0.48	-0.41		A	
G161-73	6108	3.99	-1.01	1.26	-1.18	-1.19				B	
G170-56	6112	4.11	-0.94	1.39	-0.96	-0.97	-0.62	-0.65		B	
G176-53	5615	4.52	-1.36	0.90			-0.85	-0.73		B	
G180-24	6137	4.20	-1.41	1.45	-1.17	-1.18	-0.82	-0.82		A	
G187-18	5691	4.46	-0.68	1.05	-0.44	-0.44				A	
G188-22	6116	4.20	-1.33	1.42	-1.18	-1.19	-0.68	-0.70		A	
HD3567	6180	4.01	-1.17	1.40	-1.26	-1.28	-0.83	-0.86		B	
HD17820	5873	4.28	-0.68	1.27	-0.46	-0.47	-0.18	-0.20	-0.21	C	
HD22879	5859	4.29	-0.86	1.20	-0.64	-0.64	-0.29	-0.29		C	
HD25704	5974	4.30	-0.86	1.33	-0.67	-0.68	-0.44	-0.44	-0.40	C	D
HD51754	5857	4.35	-0.58	1.30	-0.39	-0.39	-0.16	-0.17	-0.19	A	
HD59392	6137	3.88	-1.62	1.73	-1.61	-1.62	-1.12	-1.12		B	
HD76932	5977	4.17	-0.87	1.30	-0.73	-0.73	-0.37	-0.40	-0.30	C	
HD97320	6136	4.20	-1.18	1.46	-0.96	-0.97	-0.66	-0.68		C	
HD103723	6050	4.20	-0.81	1.11	-0.86	-0.86	-0.54	-0.56		B	
HD105004	5852	4.35	-0.83	1.09	-0.73	-0.73	-0.56	-0.52		B	

Table 5. continued

ID	T_{eff} (K)	$\log g$	[Fe/H]	ξ_{turb} km s ⁻¹	[C/H] LTE	[C/H] non-LTE	[O/H] ₇₇₇₄ LTE	[O/H] ₇₇₇₄ non-LTE	[O/H] ₆₃₀₀	Pop. ^a	Bin. ^b
HD106516	6327	4.43	-0.69	1.18	-0.51	-0.51	-0.11	-0.22		C	SB1
HD111980	5878	3.98	-1.09	1.39	-0.92	-0.93	-0.43	-0.46	-0.53	A	SB1
HD113679	5761	4.05	-0.66	1.37	-0.53	-0.53	-0.17	-0.19	-0.24	A	
HD114762A	5956	4.24	-0.72	1.37	-0.53	-0.54	-0.28	-0.31		C	SB1
HD120559	5486	4.58	-0.91	1.05	-0.61	-0.60	-0.39	-0.26	-0.25	C	
HD121004	5755	4.43	-0.71	1.16	-0.52	-0.52	-0.26	-0.22	-0.20	A	
HD126681	5594	4.50	-1.20	1.08	-0.98	-0.98	-0.61	-0.50		C	
HD132475	5750	3.77	-1.51	1.37	-1.35	-1.36	-0.82	-0.79		A	
HD148816	5923	4.17	-0.74	1.33	-0.53	-0.53	-0.24	-0.28		A	
HD159482	5829	4.37	-0.74	1.21	-0.54	-0.55	-0.20	-0.19		A	D
HD160693	5809	4.35	-0.48	1.02	-0.37	-0.37	-0.09	-0.10		A	
HD163810	5592	4.61	-1.22	1.17	-1.17	-1.17	-0.79	-0.67		B	D
HD175179	5804	4.40	-0.66	1.08	-0.42	-0.42	-0.09	-0.09	-0.14	C	
HD179626	5957	4.16	-1.06	1.47	-0.87	-0.87	-0.47	-0.48		A	
HD189558	5707	3.83	-1.14	1.29	-1.05	-1.06	-0.51	-0.51		C	
HD193901	5745	4.42	-1.11	1.12	-1.05	-1.05	-0.71	-0.63		B	
HD194598	6053	4.33	-1.11	1.30	-1.13	-1.14	-0.72	-0.70		B	
HD199289	5915	4.30	-1.05	1.21	-0.87	-0.88	-0.50	-0.49	-0.47	C	
HD205650	5793	4.35	-1.19	1.17	-0.94	-0.94	-0.60	-0.54		C	
HD219617	5983	4.28	-1.46	1.42	-1.53	-1.53	-0.95	-0.91		B	D
HD222766	5423	4.38	-0.70	0.75	-0.41	-0.41	-0.16	-0.07		A	
HD230409	5386	4.61	-0.87	1.01	-0.71	-0.70	-0.40	-0.27		A	
HD233511	6125	4.21	-1.58	1.20			-1.02	-0.99		A	
HD237822	5675	4.41	-0.47	0.99	-0.23	-0.23				A	
HD241253	5940	4.34	-1.11	1.17	-0.92	-0.93	-0.52	-0.51		C	
HD250792A	5572	4.50	-1.03	0.98			-0.62	-0.50		B	D
HD284248	6271	4.21	-1.59	1.51	-1.52	-1.53	-1.17	-1.15		B	

Notes. ^(a) Population classification: A, high-alpha halo; B, low-alpha halo; C, thick-disk.

^(b) Note on binarity: SB1, single-lined spectroscopic binary according to the SIMBAD database; D, double star according to the HIPPARCOS and TYCHO catalogues (Perryman et al. 1997).